Loss of multilevel 3D genome organization during breast cancer progression

Roberto Rossini, Saleh Oshaghi, Maxim Nekrasov, et al.

Genome Res. published online October 9, 2025
Access the most recent version at doi:10.1101/gr.280791.125

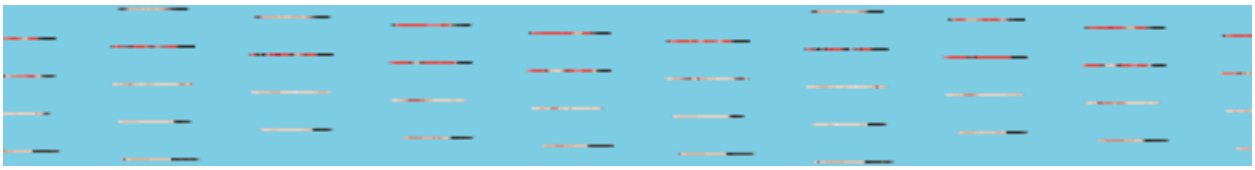

Loss of multi-level 3D genome organization during breast cancer progression

Roberto Rossini[1], Saleh Oshaghi[1], Maxim Nekrasov[2], Aurélie Bellanger[3], Renae Domaschenz[2], Yasmin Dijkwel[2], Mohamed Abdelhalim[3], Rahul Agrawal[4,5], Marit Ledsaak[4,5], Philippe Collas[3,4], Ragnhild Eskeland[5,6], David Tremethick[2]*, Jonas Paulsen[1]*

1. Department of Biosciences, Faculty of Mathematics and Natural Sciences, University of Oslo, 0316 Oslo, Norway.
2. Department of Genome Sciences, The John Curtin School of Medical Research, The Australian National University, Canberra, Australian Capital Territory, Australia.
3. Department of Molecular Medicine, Institute of Basic Medical Sciences, Faculty of Medicine, University of Oslo, 0317 Oslo, Norway.
4. Department of Immunology and Transfusion Medicine, Oslo University Hospital, 0424 Oslo, Norway.
5 Department of Molecular Medicine, Institute of Basic Medical Sciences, Faculty of Medicine, University of Oslo, 0317 Oslo, Norway.
6 Centre for Cancer Cell Reprogramming, Institute of Clinical Medicine, Faculty of Medicine, University of Oslo, 0379 Oslo, Norway.

*Correspondence: david.tremethick@anu.edu.au (DT); jonas.paulsen@ibv.uio.no (JP)

Abstract

Breast cancer entails intricate alterations in genome organization and expression. However, how three-dimensional (3D) chromatin structure changes in the progression from a normal to a breast cancer malignant state remains unknown. To address this, we conducted an analysis combining Hi-C data with lamina-associated domains (LADs), epigenomic marks, and gene expression in an *in vitro* model of breast cancer progression. Our results reveal that while the fundamental properties of topologically associating domains (TADs) are overall maintained, significant changes occur in the organization of compartments and subcompartments. These changes are closely correlated with alterations in the expression of oncogenic genes. We also observe a restructuring of TAD-TAD interactions, coinciding with a loss of spatial compartmentalization and radial positioning of the 3D genome. Notably, we identify a previously unrecognized interchromosomal insertion event, wherein a locus on Chromosome 8 housing the *MYC* oncogene is inserted into a highly active subcompartment on Chromosome 10. This insertion is accompanied by the formation of *de novo* enhancer contacts and activation of *MYC*, illustrating how structural genomic variants can alter the 3D genome during oncogenesis. In summary, our findings provide evidence for the loss of genome organization at multiple scales during breast cancer progression revealing novel relationships between genome 3D structure and oncogenic processes.

Introduction

The mammalian genome is folded into large-scale dynamic 3-dimensional (3D) chromatin conformations that provide a framework for regulated gene expression. In the interphase nucleus, chromosomes exist as territories (Rowley and Corces 2018; Cremer and Cremer 2010) within which gene-rich and active A-compartments are segregated from more gene-poor and inactive B compartments (Misteli 2004; Crosetto and Bienko 2020; Lieberman-Aiden et al. 2009), both ranging in size from single promoters up to 2 megabase-pairs (Mbp) (Sood and Misteli 2022; Harris et al. 2023). Compartments consist of multiple subcompartments that differ in their chromosomal contact frequencies, enrichment in histone modifications and chromatin-binding proteins (Spracklin et al. 2023). At a resolution ranging from ~10-800 kilobase-pairs (kbp), topologically associated domains (TADs) emerge as local, highly interacting domains (Rao et al. 2014; Nora et al. 2012; Dixon et al. 2012). TADs are further organized into sub-TADs and support the formation of internal smaller chromatin loops, which includes enhancer-promoter interactions (Berlivet et al. 2013). TADs and sub-TADs seemingly form independently of compartments (Rowley and Corces 2018). It was initially proposed that TADs provide a platform for the coordinated regulation of subsets of genes by enhancers located within the boundaries of the TAD. However, disrupting TAD structure minimally affects gene expression (Nora et al. 2017; Rao et al. 2017; Schwarzer et al. 2017), suggesting that other levels of genome organization have a more important regulatory role.

An intriguing possibility is that long-range TAD-TAD interactions, forming TAD cliques (Zhao et al. 2023; Pei et al. 2022; Li et al. 2022; Arnould et al. 2023; Paulsen et al. 2019), sculpt the 3D genome into distinct functional domains. TAD cliques are enriched in B compartments, and can gain or lose TADs during differentiation, generally in correlation with gene repression or activation, respectively (Paulsen et al. 2019). Additionally, the nuclear envelope imposes positional constraints on chromatin by anchoring heterochromatin through lamina-associated domains (LADs) of ~0.1-10 Mbp in size (Gonzalez-Sandoval and Gasser 2016; Rønningen et al. 2015; van Steensel and Belmont 2017). Accordingly, genes located at the nuclear periphery are repressed or expressed at lower levels than genes localized towards the nuclear center (Misteli 2004; Crosetto and Bienko 2020). Integrating Hi-C and LAD data allows the generation of 3D structural genome models that accurately recapitulate the radial nuclear positions of TADs (Paulsen et al. 2017, 2018; Li et al. 2017; Boninsegna et al. 2022), and provide an enhanced understanding of the link between chromatin architecture and gene regulation in disease contexts (Paulsen et al. 2017).

Indeed, transcriptional dysregulation has been attributed to alterations in 3D genome organization in diseases, including cancer (Feng and Pauklin 2020; Osman et al. 2022). Yet, analysis of multiple cancers shows that TAD boundary deletions only rarely change gene expression, emphasizing their rare involvement in gene expression dysregulation in cancer (Akdemir et al. 2023). Even with shifts in A and B compartments between colon tumors and normal intestinal cells, TADs remain relatively unchanged (Johnstone et al. 2020), suggesting compartment switching significantly impacts gene expression control (Sood and Misteli 2022; Ibrahim and Mundlos 2020).

Breast cancer is the most common cancer in women. These cancers have been classified into five subtypes based on the expression of receptors for human epidermal growth factor, estrogen and progestogen, and clinical features (Sørlie et al. 2001). Among these subtypes, triple-negative breast cancers, which do not express any of these receptors, are the most aggressive (Bobbitt et al. 2023). Few studies have examined the chromatin architectural features of breast cancer cells or tissues (Dozmorov et al. 2023; Kim et al. 2022; Wang et al.

2022; Zhou et al. 2019). Nonetheless, one study reports that triple-negative breast cancer cells display the most severe disruption of the 3D genome, including weakening of TAD borders, loss of 3D chromatin interactions leading to fewer chromatin loops, and dynamic compartmental changes (Kim et al. 2022). However, how 3D chromatin organization is associated with the progression from a normal to a breast cancer malignant state remains unexplored. Here, we rely on an *in vitro* isogenic breast cancer progression model (Dawson et al. 1996; Santner et al. 2001) to investigate 3D genome organization changes in this process.

Results

TAD properties are conserved across breast cancer stages

We performed duplicate Hi-C experiments at three stages of an *in vitro* human breast cancer progression model, corresponding to a nonmalignant state (using MCF10A cells; "10A" from here on), a premalignant state (MCF10AT1 cells; "T1") and a malignant tumorigenic state (MCF10Ca1a cells; "C1"). We obtained an average of >560 million pairwise interactions after filtering (Supplemental Table S1), supporting analyses in the range of 1-10 kbp bin resolution (Lajoie et al. 2015; Ay and Noble 2015). Filtering statistics and the relative fraction of intra- (cis) and inter- (trans) chromosomal contacts indicate high quality libraries (Lajoie et al. 2015), and samples show high reproducibility between replicates (Supplemental Fig. S1 and S2) (Yang et al. 2017). We identified and masked out regions with translocations and used ICE-normalized interactions which adjusts for bias resulting from copy-number alterations (see Methods) (Kim et al. 2022).

TAD comparisons across samples and replicates (Fig. 1A) show similar TAD numbers (~4000 TADs) and genomic size (~0.6 Mbp; Supplemental Fig. S3), TAD border insulation strength (R^2 = 0.77-1.00; Supplemental Fig. S4) and intra-TAD contact frequencies (R^2 = 0.91-1.00; Supplemental Fig. S5), and genomic positions of both TADs (Jaccard Index [JI] = 0.76-0.80; called at 50kb resolution), and sub-TADs (JI = 0.71-0.75; 10kb resolution) (Supplemental Fig. S6). Inspecting TADs surrounding known breast-cancer related genes (Lee and Muller 2010) reveals minor differences that were not consistently reproducible across replicates (Supplemental Fig. S7-S13). We conclude that TADs are overall similar across the three cell types and are therefore likely not the main oncogenic drivers in this progression model of breast cancer.

Compartments and subcompartments engage in major switching events during breast cancer progression

To map differences in long-range genome contacts in our progression model, we searched for any A/B compartment switching, a property reported to be implicated in breast cancer (Barutcu et al. 2015). Most of the genome (2124 Mbp; ~78%) remains in the same compartment across stages (Fig. 1B). However, for the fraction that switches between stages, we note 385 Mbp (~14%) in 10A switching to either B (162 Mbp; ~6%) or A (222 Mbp; ~8%) compartments in T1 (Fig. 1B; Supplemental Table S2). Most of the switched compartments remain in their switched state in C1, but a fraction switches back to B (76 Mbp; ~3%) or A (61 Mbp; ~2%). The extent of switching observed in our model is comparable to that found in other cellular contexts involving changes in cell fate (Vilarrasa-Blasi et al. 2021; Dixon et al. 2015; Liu et al. 2021), indicating that compartment switching is a prominent feature of breast cancer progression.

We next used dcHiC to identify subcompartments (Fig. 1C) (Chakraborty et al. 2022). We predict four A subcompartments (A0-A3) and four B subcompartments (B0-B3), with A1, A2 and B1 being the most prominent and A0 and B0 the least prominent for all cell stages (Supplemental Fig. S14; Supplemental Table S3). Overlaying a range of active and repressive histone modifications from public ChIP-seq datasets onto the subcompartments reveals a gradual enrichment of the ratio of heterochromatin to euchromatin features, going from B3 to A3 subcompartments (Supplemental Fig. S15). From this analysis, B2 and B3 show features of heterochromatin, with enrichment of repressive histone marks (H3K27me3) and Lamin B1. Compared to the other subcompartments, A0 and B0 are the least enriched in active and repressive histone marks respectively, raising the interesting possibility that they could be more easily remodeled into other stronger euchromatic or heterochromatic subcompartments. In contrast, A3 and B3 display the strongest active and inactive states respectively, which would arguably be more resistant to configuration changes (Supplemental Fig. S15).

Indeed, we find that (i) weaker, intermediate subcompartments (A0, A1, B0, B1) undergo more dynamic switches than more prominent and stronger subcompartments (A2, A3, B2, B3) (Fig. 1D; Supplemental Fig. S16-18). However, (ii) switching between B0 and A0 (B0↔A0) is minimal; whereas (iii) B0↔A1 is the most prominent inter-compartment switch (Fig. 1D; Supplemental Fig. S16-18), indicating specific switching between weakly heterochromatic and euchromatic states. A further characterization of paths of subcompartment switching across the three stages shows that (iv) a similar fraction of 24-26% of subcompartments ends up in either a more closed (and thus more B-like) subcompartment in C1, or a more open (A-like) subcompartment. Further, reverting back to the initial 10A-subcompartment landscape in C1 rarely happens (Supplemental Fig. S19). Lastly, (v) switches mainly involve a transition between consecutive subcompartment strengths, occurring with similar frequencies towards both more open (e.g. A2→A3) and less open (e.g. B2→B3) subcompartments (Supplemental Fig. S19). Comparing the switching levels between the two replicates shows a high degree of consistency, with coefficients of determination (R^2) ranging from 0.87 to 0.94 ($P<10^{-20}$; see Supplemental Fig. S20).

To determine implications of subcompartment switching on 3D genome organization, we generated 3D genome models (Paulsen et al. 2017) integrating Hi-C data with nuclear lamina-chromatin interactions (LADs) mapped by ChIP-seq of lamin B1 in each cell type (see Methods). The resulting models (Fig. 1E; Supplemental Fig. S21-23) display expected genomic features where more gene-poor chromosomes are located more frequently towards the nuclear periphery (Supplemental Fig. S24-26). Our 3D modeling of all three cell types reveals major differences between 10A cells versus T1 and C1 cells. As expected, there is a gradual increase in nuclear peripheral localization in subcompartments going from A3 towards B3 in 10A cells. This, however, is less apparent in T1 and C1 cells (Fig. 1F). Moreover, A3 subcompartments significantly shift away from the nuclear center in T1 and C1 cells, compared to 10A (Fig. 1F; Supplemental Table S4). B3 subcompartments appear to be slightly shifted towards the nuclear interior, which concurs with a reduction in LAD coverage in T1 and C1 cells (Supplemental Fig. S27). Taken together, our data indicate that subcompartment switching characterizing the 10A-T1-C1 cell transition is accompanied by a partial loss of radial disposition of chromatin.

Subcompartment switching reflects changes in gene expression

We next investigated whether the 3D genome structural changes observed were linked to transcriptional changes. Differential gene expression analysis from RNA-seq data between the cell types reveals 3180 differentially expressed (DE) genes between 10A and T1 cells, and

8362 DE genes between 10A and C1 cells (|LFC|>0.5; P<0.01; Supplemental Table S5). Analysis of disease-linked gene set enrichment among DE genes in T1 and C1, reveals “breast carcinoma” as the most enriched disease term, followed by other cancer types. “Organ system benign neoplasm” is the second most associated term for T1, whereas this term is absent for C1, reflecting the expected transcriptomic differences between the transformed (T1) versus the malignant (C1) cell line (Supplemental Fig. S28). Overlaying the RNA-seq data onto Hi-C-based subcompartments in all cell types reveals anticipated associations where gene expression levels gradually increase from B3 to A3 (Fig. 2A, Supplemental Fig. S29), reinforcing the validity of the subcompartment classification and the RNA-seq data in our model.

Next, we analyzed up- and downregulated DEGs in conjunction with the corresponding subcompartment switches. As expected, and as previously reported (Nagai et al. 2019; Liu et al. 2021), this analysis shows that at specific chromosomal regions (Fig. 2B), or at genome-wide levels (Fig. 2C-F), there are correlated patterns of subcompartment switching and differential gene regulation. Inspecting the presence of downregulated genes in T1 relative to 10A reveals that B1(10A)→B2(T1) is the most frequent switch for these genes (Fig. 2C left panel). Switching between B0/A0(10A)→B1(T1) or from A1(10A)→B1/B0/A0(T1) is enriched relative to what is seen for non-differentially expressed genes (Fig. 2C middle panel) or upregulated genes (Fig. 2C right panel).

To quantify whether up- and downregulated genes were associated with expected subcompartment switches towards more open (or A-like), or closed (or B-like) subcompartments, respectively, we analyzed enrichment of DE genes in each subcompartment switch relative to a switch in opposite direction. This analysis revealed a significant enrichment of downregulated genes in switching of B1→B2, B0→B1, A0→B1 and A1→B0 between 10A and T1 (all P<0.05 [binomial test]; Supplemental Table S6). Upregulated genes were significantly enriched in B1→A1, B1→B0, and A1→A3 (all P<0.05; Fig. 2C; Supplemental Table S6). Comparing 10A and C1, downregulated genes were enriched in A0→B2, A0→B1, B1→B2, and A1→A0 (all P<0.05), whereas upregulated genes were enriched in B3→B1, B1→A1, B1→A2, A0→A2, A1→A2, A1→A3 (all P<0.05; Fig. 2E; Supplemental Table S7). This suggests that specific subcompartment switching towards more open or closed states is associated with up- or downregulated DEGs, respectively.

Further, we computed the log-ratio of subdiagonal sums in the upper- compared to the lower triangular matrices from Fig. 2C. When this log-ratio is negative, DE genes are more present in 10A, and when it is positive, DE genes are more present in T1 (Fig. 2D) or C1 (Fig. 2F). We confirm switching trends towards more open subcompartments for upregulated genes, and the opposite for downregulated genes (Fig. 2D right) ($P=4.04 \times 10^{-9}$; Fisher's exact test; Supplemental Table S8), while no trend is seen for non-differentially expressed genes (Fig 2D middle). When contrasting 10A and C1, similar trends are seen (Fig. 2E-F; $P=6.66 \times 10^{-13}$; Supplemental Table S9). Thus, subcompartment switching aligns with changes in gene expression.

Reorganization of TAD-TAD interactions coincides with subcompartment alterations

Beyond their subcompartment organization, we have previously shown that TADs can arrange in densely interconnected long-range contact configurations termed TAD cliques (Paulsen et al. 2019). To identify these cliques, each TAD is represented as a node in a graph, with edges indicating statistically significant Hi-C interactions between pairs of TADs. We define a "TAD clique" as a maximal, fully-connected subset of nodes that cannot be expanded without losing full connectivity, which is identified using the Bron-Kerbosch algorithm (Bron and Kerbosch

1973). The size of a TAD clique is the number of nodes in a maximal clique (see Fig. 3A inset, and Supplemental Fig. S30). We computed TAD cliques in 10A, T1 and C1 cells (see Fig. 3A-B), and found that the distribution of maximal clique sizes overall show an expected decrease in their frequency as their size increases (Fig. 3A; Supplemental Fig. S31A). Notably, in 10A TAD cliques of size 3 are 17% less frequent than in T1 ($P=0.023$; Suppl. Table S10), and 24% less frequent than in C1 ($P=7.3 \times 10^{-8}$; Suppl. Table S10). Larger TAD cliques (size>4) on the other hand seem generally more enriched in 10A, than in T1 and C1. T1 generally exhibits fewer TAD cliques than 10A and C1 (Fig. 3A). Therefore, larger clique sizes are more apparent in normal 10A cells. These observed trends and differences are likely not related to structural variants in the T1 and C1 cells, as masking these out reveals similar distributions as in non-masked data (Supplemental Fig. S31).

We overlapped TAD cliques of different sizes with subcompartments, and observed that association of B-type subcompartments increases with TAD clique size (Supplemental Fig. S32). To characterize TAD clique dynamics, we analyzed alterations in TAD maximal clique sizes across cell types (Fig. 3C-D; Supplemental Fig. S33-S39). A large fraction of TADs do not engage in cliques (Fig. 3C). However, those TADs that do form cliques grow or decrease in size (Fig. 3C-D; Supplemental Fig. S33-S39) across all stages. Thus, like subcompartments, TAD cliques also reconfigure extensively in this model system of breast cancer progression.

Our previous observations do not exclude the possibility that growing TAD cliques involve TADs of various chromatin composition, thus belonging to various subcompartments. To explore this, we used HDBSCAN (McInnes et al. 2017; McInnes and Healy 2017) to cluster each clique based on their TAD-wise enrichment in subcompartments. Clustering was performed targeting clusters with a minimum cluster size of 200 TAD cliques, plus a cluster dedicated to collect outliers (see Methods for more details). The resulting nine clusters (Fig. 3E) show that individual TAD cliques frequently involve multiple types of subcompartments (Supplemental Fig. S40), and thus represent a level of TAD association where subcompartments of different types potentially intermix.

To investigate the dynamics of TAD clique clusters, we explored the frequency of each of the nine TAD clique clusters in each cell type (Fig. 3F; Supplemental Table S11). We find that most clusters display a cancer progression stage-specific association, such that a cluster tends to be more enriched in one or two of the three cell types examined here (Fig. 3E,F). Some clusters involving B-type subcompartments (Cluster 0 and 2) appear to be significantly more prevalent in T1 and C1 compared to 10A. Conversely, some clusters with A-type subcompartments (Cluster 1, 5-7) seem to be diminished in T1, but exhibit partial recovery in C1 (Fig. 3F; Supplemental Table S12). These are also clusters enriched in weaker, intermediate subcompartments, which could reflect their increased switching.

In summary, TAD cliques bring together TADs overlapping with various subcompartments, which differ in 10A, T1 and C1 cells. Overall, this signifies the role of subcompartment alterations and intermixing during breast cancer progression in this model system.

Interchromosomal insertion of the *MYC* locus coincides with de novo enhancer contacts and oncogene activation

As expected, the cell types used in our breast cancer progression model harbor structural variations (SVs), including copy number alterations, insertions, deletions and translocations. We exploited the ability of Hi-C to detect many of these SVs, to call SVs genome wide (Supplemental Fig. S41-S43). We manually inspected the called variants and confirmed known SVs (Santner et al. 2001), including t(3;9), t(3;5), t(3;17), t(6;19). In addition, we

identified previously undescribed SVs, including t(7;9) and t(10;17). Analyzing the 3D structural consequences of all SVs in these cell lines is computationally infeasible. Nevertheless, to investigate 3D genome consequences of select SVs, we focused on a striking pair of regions on Chromosome 8 (126330000-128235000 bp; hg38) (Fig. 4A) and Chromosome 10 (71280000-73310000 bp; hg38) (Fig. 4B). Both regions show a gradual and coordinated increase in copy number, going from T1 to C1 (Fig. 4A,B). A large region at the end of Chromosome 8 is amplified in 10A, but not in T1 and C1 (Fig. 4A). The region on Chromosome 8 is well-characterized (Visscher et al. 1997; Grisanzio and Freedman 2010) and contains several breast cancer related genes. These notably include *MYC*, an oncogenic transcription factor with a pivotal role in breast cancer progression (Liao and Dickson 2000) and whose amplification and overexpression is a marker of aggressive and invasive breast cancer (Corzo et al. 2006; Berns et al. 1992).

Further inspection of the Hi-C data at the intersection of these two regions in the Hi-C matrix reveals, after ICE balancing, an enrichment of contacts of the region towards the entire Chromosome 10, clearly indicating that the *MYC* locus is inserted in the Chromosome 10 region (Fig. 4C). Enriched contacts with other chromosomes are also seen, due to the amplification of the locus (Fig. 4C). Zooming in on the specific interchromosomal contacts between the *MYC*-locus and the locus on Chromosome 10, we note Hi-C patterns that typically suggest chromatin looping and extrusion of intra-chromosomal DNA (Fig. 4D). This again indicates an insertion event. Investigating the region using a different balancing scheme which explicitly models and accounts for copy number alterations (Servant et al. 2018) reveals similar trends. This indicates that the copy number alterations themselves are not distorting the Hi-C data in this region (Supplemental Fig. S44). Comparing the contact maps between the three cell types reveals that the insertion is novel in the T1 and C1 cells (Supplemental Fig. S45).

We next examined the chromatin context of this insertion event. Inspection of subcompartments in this region shows that the insertion site on Chromosome 10 is nearly entirely covered by A3-subcompartments (Supplemental Fig. S46A) in all three cell types, indicating that the *MYC* locus is inserted into a highly active genome region on Chromosome 10. Initially, the *MYC* gene resides in an A2 subcompartment on Chromosome 8 in the 10A cell line. However, it switches to a more active or “open” state (A2→A3) in T1 and C1 (Supplemental Fig. S46B).

Next, we assessed the nature of the *de novo* contacts detected between the *MYC* locus and sites on the host Chromosome 10. To this end, we overlaid positions of MCF10A enhancers predicted from EnhancerAtlas 2.0 (Gao and Qian 2020) onto the Chromosome 8 and 10 amplification unit (Fig. 4D; green segments). The four distinct *MYC* interactions detected in the Hi-C map (Fig. 4D, circles) evidently corresponds to (i) two *de novo* contact points between enhancer elements on Chromosome 10 and the *MYC* promoter, and (ii) an interaction with enhancer elements ~1 Mbp upstream of the *MYC* promoter (Fig. 4D). Generating a virtual 4C plot (Sexton et al. 2012) (see methods) anchored at the *MYC* locus, confirms that the enrichment of contacts towards these putative enhancer elements is specific to T1 and C1 (Fig 4D; bottom track).

To validate the *de novo* interactions (proximity) of the *MYC* gene with elements on Chromosome 10 at the cellular level, we carried out a fluorescence in situ hybridization (FISH) analysis of the relative positions of the *MYC* gene (*‘MYC’* probe on Chromosome 8 at position 127543567-127702694) and either a *de novo* interacting enhancer on Chromosome 10 (“Chr10 enhancer” probe at position 73117711-73267436), or another site on Chromosome 10 ~500 kbp downstream (“Chr10 downstream” probe at position 73794997-73992612; see Methods). The data show that both the *“MYC*-Chr10 enhancer” and the “*MYC*-Chr10 distal”

distances are significantly shorter in C1 cells than in 10A cells ($P=1.9 \times 10^{-14}$ and 1.3×10^{-7} respectively; Fig. 4E,F; Supplemental Fig. S47A-D), yet the *MYC* enhancer contact is significantly shorter than the distal interaction ($P=9.3 \times 10^{-6}$). These findings support the view that the *MYC* locus has undergone an insertion into Chromosome 10 in C1 cells. Furthermore, this region harbors enhancer elements which may interact with *MYC*, though resolution limitations of our FISH probes prevent a more detailed characterization.

Furthermore, to provide an element of functional significance to this *MYC* insertion, we examined RNA-seq data for these two regions. The data show an upregulation of breast cancer related genes in T1 and C1 relative to 10A, including *LRATD2, PCAT1, CASC19, CASC8, POU5F1B, PVT1* and *MYC* on Chromosome 8. Several breast cancer related genes in the Chromosome 10 region are also upregulated, such as *UNC5B, CDH23, PSAP, SPOCK2, ASCC1, DDIT4, NUDT13, ECD, DNAJC9* and others (Supplemental Table S13 and S14).

To dissect the functionality of the *MYC* insertion we designed 5´ and 3´sgRNA pairs to target the de novo putative enhancer interactions (Supplemental Fig. S48A). The *MYC* de novo contacts are proximal to the *DNAJC9* locus on Chromosome 10 (Figure 4D), where three putative cis regulatory elements (REs) enriched in ENCODE H3K27ac and annotated CREs are found (REs 1-3; Supplemental Fig. S48B). Virtual 4C-track overlays reveal enriched contacts in T1 and C1 cells compared to 10A within this region, with a peak aligning with RE1 (Supplemental Fig. S48B; top). C1 cells were double transfected with pLentiMultiCRISPR vectors where Cas9 is coexpressed with puromycin and each sgRNA pair to create six different genomic deletions spanning RE 1-3 (Supplemental Fig. S48B) or sgRNAs for mCherry or EGFP as controls. The Cas9 protein was equally expressed from all vectors in C1 cells compared to GAPDH (Supplemental Fig. S48C). After two days of puromycin selection for Cas9 expressing C1 cells, we observe a subtle, yet not significant, decrease in *DNAJC9* expression upon Cas9 targeting of the three REs in the locus (Supplemental Fig. S48D). *MYC* expression slightly decreased in C1 cells expressing guide pairs for deletion of RE1.1 and RE1.2, and showed a subtle increase in expression for sgRNAs surrounding RE2.1-2 and RE3.1-2, yet not statistically significant (Supplemental Fig. S48E). We did not observe any change in expression of *POLR2A*, encoding for the largest subunit of RNA polymerase II on Chromosome 17 upon targeting of Cas9 to REs 1-3 or controls (Supplemental Fig. S48F). To evaluate Cas9 editing efficiency, we amplified genomic DNA from puromycin-selected, doubly transfected C1 cells using primers targeting regions surrounding sites recognized by sgRNAs in RE1, 2 or 3 (Supplemental Fig. S49A). PCR products were analyzed by gel electrophoresis, purified, and sequenced (Supplemental Fig. S49B). This evaluates the frequency of indels surrounding each of the sgRNA breakpoints, which was quantified using the TIDE method (Brinkman et al. 2014), and found to be relatively low (0.8–7.6%; Supplemental Table S19). This may partially explain the subtle effect on *MYC* expression and low Cas9 deletion frequency of RE1-3. However, the genomic complexity and redundancy of the *MYC* locus make definitive conclusions challenging.

Collectively, these observations indicate that the *MYC* locus has not only been amplified but also inserted into a transcriptionally active region of Chromosome 10 in C1 cells, with the formation of de novo cis-contacts between *MYC* and regulatory elements in the host chromosome. Upregulation of *MYC* and of other breast cancer-related genes in malignant C1 cells speculatively suggests functionality of these de novo interactions, yet determination of any involved enhancer elements remains. Our results highlight how structural variants in the genome may cooperate with 3D genomic states during oncogenesis.

Discussion

The intricate 3D organization of the genome plays a pivotal role in gene regulation and cell function. Using a multilayered (epi)genomic approach, we report here for the first time, to our knowledge, significant alterations in higher-order 3D chromatin organization in an *in vitro* breast cancer progression model.

First, major compartment and subcompartment switching emerges as a prominent dynamic feature, which as expected based on previous studies (Nagai et al. 2019; Liu et al. 2021), correlates with altered expression of genes implicated in breast cancer. Second, we identify a reconfiguration of preferred associations between TADs, or TAD cliques (Paulsen et al. 2019), which bring together new A- and B-type subcompartment associations. Third, spatial subcompartment organization changes in the pre-malignant and malignant states potentially also contribute to the loss of gene expression control. Collectively, there is a coordinated and progressive reorganization of higher-order genomic structure to an abnormal state. However, casual relationships remain to be determined.

The extent of compartment switching observed in our model (22%) is similar to what is seen during B cell differentiation (28.1%) (Vilarrasa-Blasi et al. 2021), although the latter includes an additional intermediate compartment, inflating the percentage. In contrast, 7.5% of the genome harbors statistically significant compartment switches during differentiation of mouse embryonic stem cells (ESCs) into neuronal progenitors (Chakraborty et al. 2022). A/B-compartment switching varies between 8-36% comparing various ESC-derived cell types (Dixon et al. 2015; Liu et al. 2021). Comparatively, this indicates that the level of switching observed in our oncogenic model is substantial.

Our study did not uncover involvement of substantial TAD border dynamics in the in vitro progression model of breast cancer. However, we cannot entirely rule out its subtle involvement due to minor differences in consistency across replicates. Further investigation of these differences is needed to uncover any potential functional consequences. Additionally, the potential role of cell heterogeneity in cancer cells cannot be dismissed, given that our data represent an overall behavior in bulk cell populations (Zhu et al. 2023). This heterogeneity is expected to primarily affect 3D genome models, but single-cell copy number variations could also influence estimates of overall copy numbers.

A new observation from our data is a previously unknown insertion of the *MYC* locus (normally localized on Chromosome 8) into highly active A3-subcompartments on Chromosome 10. This is accompanied by *de novo* interactions correlating with not only elevated *MYC* expression in T1 and C1 cells, but also with enhanced expression of other breast cancer related genes on both chromosomes. Our FISH analysis supports our Hi-C findings of *de novo* interactions between *MYC* and a region harboring enhancer elements on Chromosome 10 in C1 cells, but not in 10A cells. Furthermore, a complementary study has also classified this insertion as an enhancer hijacking event (Wang et al. 2021). Notably, in murine B cells, *MYC* has been shown to relocate to active transcription factories in proximity to *IGH,* a frequent translocation partner (Osborne et al. 2007). However, our FISH results indicate that in 10A cells, *MYC* is not proximal to the Chromosome 10 locus, suggesting *MYC* is not part of a transcription factory with this locus prior to the insertion event. Our analyses did not test for changes in *MYC* location in response to signaling pathway activation as in (Osborne et al. 2007), and thus refer to a "baseline" situation in these cells.

Identifying enhancer candidates from Hi-C interactions is challenging due to the data's low genomic resolution in pinpointing enhancer-promoter contacts. Tools like 4C and Micro-C can provide higher-resolution insights into specific chromatin interactions. However, these

techniques do not guarantee that detected contacts correspond to functional interactions, as spatial proximity does not inherently imply biological significance (Splinter et al. 2012; Hsieh et al. 2020).

Focusing on three regulatory elements (REs1-3) in the *DNAJC9* locus on Chromosome 10 intersecting the central part of the "dot" observed in our Hi-C data (Fig. 4D), we utilized a CRISPR-Cas9 strategy to analyze consequences of deleting these putative enhancer elements in C1 cells. From this, we observed changes in expression of *DNAJC9* and *MYC* compared to sgRNA controls, yet these changes were not statistically significant. Studies have shown that deleting individual enhancers can have minimal impact due to redundancy among enhancers and may cause only transient effects (Osterwalder et al. 2018; Diao et al. 2016), possibly explaining why targeting individual *DNAJC9* REs may have low effect on MYC expression. These effects may, however, also be masked by the large copy numbers of *MYC* and *DNAJC9* loci (Fig. 4A,B). Moreover, the low editing efficiency of individual sgRNAs in pool C1 cells after transient transfection and puromycin selection suggest a low frequency of the RE1-3 deletions (Supplemental Table S19). Therefore, we cannot definitively determine the functional significance of the observed enhancer interactions.

The detailed spatial configuration of this insertion remains unclear, but there are several possibilities. The mirror-symmetry and isolated contact map of the Chromosome 10 segment with specific regions of the Chromosome 8 segment (see Fig. 4D), featuring stripes, could suggest that the region exists as circular, extrachromosomal DNA (ecDNA). The formation of ecDNA structures is a common form of oncogenic amplification, and often occurs around *MYC (Hung et al. 2022; Hoff et al. 1988)* to promote functional *cis*-regulatory contacts (Morton et al. 2019). However, the focal and limited MYC probe signals (Supplemental Fig. S47A-B) are inconsistent with an ecDNA event (Hung et al. 2021), leaving the structural interpretation unresolved.

Beyond our identified interchromosomal insertion of the *MYC* locus, the intricate aneuploidy patterns commonly observed in cancer pose a challenge that existing standard software and pipelines struggle to effectively address. Promising strides have been made using long-read Hi-C technology (Garg 2023) or statistical approaches (Brunette et al. 2024) to alleviate this issue. Nevertheless, a significant gap remains in the availability of computational pipelines tailored for comprehensive downstream analysis of reordered cancer genome data relative to a karyotypically normal reference genome. This needs to be addressed if further progress in understanding the 3D cancer genome is to be achieved.

In conclusion, our findings provide new insights into the complex genomic structural changes that underlie breast cancer metastatic progression. The interplay between subcompartment switching, LAD-linked subcompartment spatial nuclear reorganization, and TAD clique dynamics represents a multifaceted mechanism by which the 3D genome can be abnormally and dynamically reconfigured during breast cancer development. Targeting these 3D genome alterations could potentially lead to improved or new therapeutic strategies to better treat breast cancer in the future (Park et al. 2023).

Methods

Cells

MCF10A, MCF10AT1, and MCF10Ca1a cell lines were grown in DMEM/Nutrient F12 (DMEM/F12) media supplemented with 5% horse serum (MCF10A and MCF10Ca1a) or 2.5% horse serum (MCF10AT1), 14 mM NaHCO3, 10 µg/mL insulin, 2 mM L-glutamine, 20 ng/mL human epidermal growth factor, 500 ng/mL Hydrocortisone and 100 ng/mL cholera Toxin.

MCF10A cells were obtained from the American Type Culture Collection (CRL-10317). MCF10AT1 and MCF10Ca1a cells were obtained from the Barbara Ann Karmanos Cancer Institute (Detroit, Michigan).

Fluorescence in situ hybridization (FISH)

FISH was done as exactly described by us previously (Paulsen et al. 2017). In short, MCF10A and MCF10Ca1a cells were incubated in a hypotonic buffer, fixed in ice-cold methanol:acetic acid and dropped on glass slides. BAC FISH probe DNA (BacPac Resource Center) was labeled using a Nick Translation Kit (Roche). The following probes were used:

- '*MYC*' gene probe: clone ID RP11-1136L8; Chr.8; position 127543567-127702694
- 'Chr. 10 enh.' enhancer probe: clone ID RP11-152N13; Chr.10; position 73117711-73267436
- 'Chr. 10 distal' probe: clone ID RP11-390A15; Chr.10; position 73794997-73992612

The MYC gene probe was labeled with Digoxigenin-11-dUTP (Roche). The Chr.10 enhancer and Chr.10 distal probes, both positioned to mark sites expected to be proximal to the *MYC* gene on Chromosome 10) were labeled with Biotin-16-dUTP (Roche). For each slide, 200 ng of each 'MYC gene' + 'Chr.10 enhancer' probe, or 'MYC gene' + 'Chr.10 distal' probe were mixed with 30 µg of Cot-1 DNA and 150 µg salmon sperm DNA and precipitated. DNA was dissolved in hybridization mix and pre-annealed for 1 h. Slides were RNase-treated, washed, dehydrated in ethanol, denatured, and dehydrated again.

Probes were denatured, pre-annealed and applied onto cells for overnight hybridization at 37°C. Slides were then washed in 2× SSC and in 0.1× SSC, blocked in 5% skim milk and incubated with Anti-Digoxigenin (Roche; mouse; 0.4 µg/ml). Slides were washed, incubated with Avidin Alexa Fluor 488 conjugate (Invitrogen; 1.7 µg/ml) and Alexa Fluor® 594-conjugated Anti-Mouse (Jackson ImmunoResearch; rabbit; 2.5 µg/ml), washed and incubated with Biotinylated Anti-Avidin D conjugate (Vector; goat; 1.0 µg/ml) and Alexa Fluor® 594-conjugated Anti-Rabbit (Jackson ImmunoResearch; donkey; 2.5 µg/ml). Slides were washed and incubated 30 min with Avidin Alexa Fluor 488 conjugate (Invitrogen) (1.7 µg/ml). Slides were mounted with 0.2 µg/ml DAPI in Dako Fluorescent Mounting Medium. Images taken under a 100× objective (numerical aperture 1.4) mounted on an IX71 inverted microscope (Olympus) fitted with the DeltaVision wide-field imaging station (GE Healthcare).

Hi-C

HiC Libraries were prepared in duplicates for each cell type using the Arima-HiC+ kit (Arima Genomics, USA) according to manufacturer instructions. For each cell line (10A, T1, C1) 1 million cells were used per HiC reaction. Cells were fixed with 1.2% formaldehyde for 12 min. All subsequent steps were carried out according to the Arima protocol. Resulting libraries were amplified with 5 PCR cycles and sequenced on an Illumina NovaSeq 6000 instrument in paired-end run with 2×101 bp.

RNA-seq

All mRNA-seq experiments were performed in triplicate. Total RNA was isolated using the Qiagen RNeasy kit following manufacturer's instructions. Stranded mRNAseq libraries were constructed using Illumina mRNA Prep kit, following vendor protocol with poly(A) enrichment (Illumina). Libraries were sequenced with 2×75bp paired-end on an Illumina NextSeq 500.

CRISPR-Cas9 Regulatory element deletions

Paired sgRNAs (5´and 3´- sgRNAs) were designed to target both ends of selected candidate regulatory elements (REs) in the human *DNAJC9* locus to create a deletion. sgRNA with on-target high predicted cleavage and low number of off-targets were carefully selected using UCSC Genome Browser (hg38) (Perez et al. 2025) CRISPR Target track based on CRISPOR (Haeussler et al. 2016). The sgRNAs were cloned stepwise into Lenti-multi-CRISPR plasmid that contains human codon-optimized *Streptococcus pyogenes* Cas9 (spCas9) followed by a *porcine teschovirus-1* 2A peptide (P2A) self-cleavage sequence upstream of the puromycin sequence (Addgene plasmid # 85402) (Cao et al. 2016). The first gRNA was cloned by insertion of two annealed complementary oligonucleotides into the BsmBI site using the Infusion cloning approach (TaKaRa Clontech, Supplemental Table S20). The plasmid containing one guide was opened with NheI (NEB) and a DNA fragment containing U6 promoter, sgRNA and scaffold (IDT technologies) was inserted by infusion cloning (Supplemental Table S19). A total of two sgRNA pairs per three *DNAJC9* locus REs were cloned. sgRNAs for mCherry and EGFP were designed as negative controls and inserted separately as annealed oligonucleotides by infusion cloning into the BsmBI site in two separate Lenti-multi-CRISPR plasmids. All plasmids were fully sequenced by Oxford Nanopore technology (Eurofins Genomics) and the sequences manually verified.

A total of 600,000 C1 cells were seeded per six well in DMEM/F12 supplemented media as described above. After 24 hours, three technical replicates of six wells were transfected with 2.5 µg of Lenti-multi-CRISPR plasmid containing 5´ and 3´-sgRNA RE pair or EGFP sgRNA or Cherry sgRNA using Lipofectamine 3000 (Thermo Fisher Scientific). At 24 hours post transfection, each 6 well was transfected again with 2.5 µg of the same sgRNA-Lenti-multi-CRISPR plasmid using Lipofectamine 3000. After 24 hours, the double transfected C1 cells were selected with 4 µg/ml of puromycin for 48 hours. Onday five, the media was changed and the cells left to recover. On day six, the six wells were washed in 1 x PBS and either collected in 500 ul TRIzol Reagent (Thermo Fisher Scientific) for total RNA or trypsinized and pelleted for genotyping. Genomic fragments spanning sgRNAs in RE1, 2 or 3 were amplified by Q5 polymerase (NEB), single bands were purified and sanger sequenced (Eurofins) (Supplemental Table S20). The TIDE web tool (version 3.3.0) (Brinkman et al. 2014) was used to determine the efficiency of individual guide RNAs in generating targeted indel mutations in a cell population at 25 nucleotides from the breakpoint (Supplemental Table S19).

To verify Cas9 expression, whole cell lysates of C1were lysed in 2x SDS loading dye and loaded on a an 4-20% SDS PAA gel (BioRad) after lipofectamine transfection with pLentiMultiCRISPR (addgene #85402) with sgRNA pairs spanning RE1.1, RE1.2, RE2.1, RE2.2, RE3.1, RE3.2, and guide controls against EGFP and mCherry. Whole cell lysates from C1 cells transfected with a vector with humanized Cas9 (hCas9, addgene #41815) was loaded as control (Mali et al. 2013). The proteins were transferred to a PVDF membrane (Millipore) and detected with anti-Cas9 (Cas9-clone 7A9 Cat # MAC133, Sigma Aldrich, expected size 160 kda) and anti-GAPDH (Novus biologicals, expected size 37 kda) as a loading control followed by secondary IR800 donkey anti-mouse and IR680 donkey anti-goat (LicorBiO) and detected by an OdysseyDLx imager.

Total RNA from the three six wells for each 5´and 3´- sgRNA pair or control EGFP/ mCherry sgRNAs Lenti-multi-CRISPR plasmid transfected cells was purified using a RNeasy kit with an on-column DNase I treatment according to manufacturer's protocol (Qiagen). RNA was eluted in 25 µL ddH2Oquantified using NanoDrop and quality controlled by agarose gel electrophoresis. A total of three different replicates of double transfections with puromycin treatment conducted at different times were processed. 2 mg of total RNA was

used for generation of cDNA primed with oligo(dT) according to manufacturer's instructions (AffinityScript cDNA synthesis kit Cat # 600559, Agilent).

The endogenous *MYC*, *DNAJC9*, *RPL30* and *POL2RA* mRNA expression levels were measured by quantitative RT-PCR using EvaGreen dye (Biotium) on a BioRad CFX Real-Time System. A standard curve was generated for each primer set with Thermal cycle conditions for 40 PCR cycles (95° for 12 min, 95° for 15s, 65° for 30s, 72° for 30s) (Supplemental Table S19). The Real-Time Efficiency (%) for each primer pair was calculated according to E = -1+10(-1/slope) (Rasmussen 2001) and converted primer efficiency = E (%)/100 +1.

Three technical replicates were run per qRT-PCR (n=3 rounds of CRISPR; (n=9 technical replicates)). Relative gene expression was analyzed using Pfaffl's mathematical model (Pfaffl 2001) for 5´and 3´- sgRNA RE pair or mCherry sgRNA versus EGFP sgRNA transfected cells normalised to housekeeping gene RPL30 as reference:

$$Ratio\ (RQ) = (E_{target\ gene})^{\Delta C(targe\ genet)} / (E_{reference})^{\Delta C(reference)}$$

ΔCt(target) = Ct(Mean target gene in CRISPR control gRNA(EGFP) cells)−Ct(target gene in CRISPR RE or mCherry sgRNA cells)
ΔCt(reference) = Ct(reference gene in CRISPR control gRNA(EGFP) cells)−Ct(reference gene in in CRISPR RE or mCherry sgRNA cells)

Ratio was calculated for average of technical Cp values per replicate, then these were averaged and STDEV calculated. The control sample was from pooled cells transfected with EGFP gRNA. Samples are RE = Pool of cells with guide pair for RE1.1; RE1.2; RE2.1; RE2.2; RE3.1 or RE3.2. A pool of cells with mCherry gRNA acts as a negative CRISPR control. Target genes are MYC, DNAJC9 and POLR2A (internal control target gene on chromosome 17, assumed not affected by CRISPR deletions). qRT-PCR data statistical analysis and plots were performed on GraphPad Prism 10.4.1. For statistical evaluations of the determined CP variations and calculated relative expression variations, data were analysed for significant differences by one-way ANOVA using Dunnett's multiple comparisons test between mCherry sgRNA and each of different RE guide pairs were performed on GraphPad Prism v 10.4.1 (Supplemental Table S20, the confidence level was set to 0.05).

ChIP-seq of lamin B1 and mapping of lamina-associated domains (LADs)

ChIP of lamin B1 was done as described by us (Rønningen et al. 2015). In short, cells were cross-linked with 1% formaldehyde, lysed in 50 mM Tris-HCl pH 7.5, 10 mM EDTA, 1% SDS and protease inhibitors, and sonicated in a Bioruptor (Diagenode) into ~200-bp fragments. After sedimentation, the supernatant was diluted tenfold in the RIPA buffer. Chromatin was incubated overnight at 4°C with antibodies to lamin B1 (10 µg per 10 million cells; Abcam, ab16048), coupled to Invitrogen Dynabeads protein A/G (Thermo-Fisher). ChIP samples were washed four times in ice-cold RIPA buffer, after which cross-links were reversed and the DNA was eluted for 6 h at 68°C. DNA was purified using phenol–chloroform isoamylalcohol and dissolved in H_2O. ChIP-seq libraries were prepared using the Diagenode Microplex library preparation kit v2 and TruSeq LT indexes, and samples were sequenced (single-end) on an Illumina HiSeq 4000.

ChIP sequence reads were mapped to hg38 with Bowtie 2 v2.4.1 (https://github.com/BenLangmead/bowtie2) (Langmead and Salzberg 2012) after removing

duplicates using Picard MarkDuplicates (http://broadinstitute.github.io/picard/). Reads from both input samples were merged, mapped to hg38 and duplicates removed as above. To alleviate normalization bias, each pair of mapped ChIP and input read files contained the same read depth after down-sampling reads for each chromosome. Mapped reads were used to call LADs from ten consecutive runs of Enriched Domain Detector (EDD) (http://github.com/CollasLab/edd) (Lund et al. 2014) with auto-estimation of GapPenalty and BinSize, and mean GapPenalty and BinSize values were used for a final EDD run (Forsberg et al. 2019). Final LADs for each cell type were the union of the three replicates.

Structure of code used for data analyses

Source code used to produce all results presented in this paper (except LADs analysis and downstream analysis of Chrom3D models) is hosted on GitHub at github.com/paulsengroup/2022-mcf10a-cancer-progression and is archived on Zenodo at the following DOI: 10.5281/zenodo.17121063.

Most of the computation is organized into Nextflow workflows, with each workflow performing a subset of the data analysis (e.g. the differential expression and comparative analyses are performed by two different workflows).

All workflows mentioned in the method sections are hosted on the GitHub repository inside folder workflows/. Scripts and Jupyter notebooks are found under folders bin/ and notebooks/, respectively.

Some of the analysis steps required us patching third party tools. The patches are described in section Software patches and patch files are available on the GitHub repository under container/patches/. All our patches were contributed upstream. Most of our patches were accepted by upstream and are already part of a stable release. Figures were produced directly by workflows or using scripts and notebooks under bin/plotting and notebooks/, respectively. The final version of figures were produced by assembling draft images with Inkscape and Omnigraffle.

Data analysis workflows were run on a HPC cluster using Apptainer (Kurtzer et al. 2017).

Hi-C preprocessing

We used a modified version of nf-core/hic v2.0.0 (https://zenodo.org/records/2669513) (Ewels et al. 2020; Servant et al. 2015; Ewels et al. 2016; da Veiga Leprevost et al. 2017) for quality control, sequence mapping and filtering using hg38.p14 (International Human Genome Sequencing Consortium 2001). The workflow was run using restriction enzymes for the 2-enzyme Arima Kit (--restriction_site="^GATC,G^ANTC" and --ligation_site="GATCGATC,GANTGATC,GANTANTC,GATCANTC"). The following optional flags were specified: --skip_maps, --skip_dist_decay, --skip_tads, --skip_compartments, --skip_balancing, --skip_mcool, --split_fastq=false. The .chrom.sizes file given to nf-core/hic was filtered to only retain chromosome sequences using grep '^chr[[:digit:]XY]\+[[:space:]]'. Chromosomes were sorted by name using gnu sort -V. The output of nf-core/hic was compressed using workflow robomics/compress-nfcore-hic-output v0.0.1 (https://zenodo.org/records/7949266). Hi-C contact matrices in multi-resolution Cooler format were generated using a patched version of cooler v0.9.1 (Abdennur and Mirny 2020). We used cooler cload to ingest interactions in .validPair format into a .cool file at 1 kbp resolution. We then converted the .cool file to .mcool file format using cooler zoomify. Finally, matrices were balanced with several methods using juicer_tools v2.20.00 (Durand et al. 2016) (VC, KR, SCALE methods using intra-chromosomal, inter-chromosomal and genome-wide interactions), and cooler (ICE method using intra-chromosomal, inter-chromosomal and

genome-wide interactions) (Abdennur and Mirny 2020). Regions overlapping centromeres and assembly gaps for hg38 were masked before balancing (files retrieved from UCSC FTP server on 2023/02/24). Downstream analyses were performed using cis-only, ICE balanced matrices unless otherwise specified. For some analyses, replicates for the same condition were merged to generate deeper Hi-C matrices using cooler merge (Abdennur and Mirny 2020). The resulting matrices were then coarsened and balanced cooler and juicer_tools as outlined above (Abdennur and Mirny 2020; Durand et al. 2016). All the above steps were performed by running script run_nfcore_hic.sh, which runs workflow postprocess_nfcore_hic.nf after running nf-core/hic. Fig. S1 was generated by workflow postprocess_nfcore_hic.nf based on the output of nf-core/hic. Fig. S2 was generated by workflow comparative_analysis_hic.nf by running the Python implementation of HiCRep v0.2.6 (Lin et al. 2021; Yang et al. 2017). Correlation values shown in the plot were computed as the weighted average of the correlation coefficient of each individual chromosome using chromosome sizes as weights. Individual correlation coefficient values are available in Supplemental File S1.
In addition, interactions involving Chromosome 8 and Chromosome 10 were balanced with LOIC using the iced package (v0.5.10) (Servant et al. 2018). LOIC balancing is performed in one of the steps of the comparative_analysis_hic.nf workflow.

RNA-seq preprocessing

We used nf-core/rnaseq v3.12.0 (https://zenodo.org/records/7998767) to perform quality control, trimming, alignment and generating the gene expression matrix (Ewels et al. 2020; Di Tommaso et al. 2017) (Ewels et al. 2020; Di Tommaso et al. 2017); This includes the following tools: featureCount (Liao et al. 2014); GffRead (Pertea and Pertea 2020); MultiQC (Ewels et al. 2016); preseq (Daley and Smith 2013); Qualimap 2 (Okonechnikov et al. 2016) ; RSeQC (Wang et al. 2012); Salmon (Patro et al. 2017); SortMeRNA (Kopylova et al. 2012); STAR (Dobin et al. 2013); StringTie2 (Kovaka et al. 2019); UCSC Tools (Kent et al. 2010); DESeq2 (Love et al. 2014); dupRadar (Sayols et al. 2016); Tximeta (Love et al. 2020); Bioconda (Grüning et al. 2018) ; Biocontainers (da Veiga Leprevost et al. 2017) and Apptainer (Kurtzer et al. 2017). nf-core/rnaseq was run using hg38.p14 as reference genome (International Human Genome Sequencing Consortium 2001). The FASTA file used as reference was first filtered using SeqKit v2.5.1 (Shen et al. 2016) to remove mitochondrial chromosomes and unplaced scaffolds by using the following pattern '^chr[XY\d]+$'. We used the genome annotation for hg38 from GENCODE v43 (Frankish et al. 2019). The pipeline was launched using the following optional flags: --aligner=star_salmon, --pseudo_aligner=salmon, --extra_salmon_quant_args='--seqBias --gcBias', --gencode=true.
The workflow was run by launching script run_nfcore_rnaseq.sh.

ChIP-seq analyses of public datasets

We used nf-core/chipseq v2.0.0 to perform quality control, mapping, filtering and peak calling of publicly available ChIP-seq datasets from MCF10A cells (Ewels et al. 2020; Di Tommaso et al. 2017). This includes the following tools: BWA (Li and Durbin 2009); BEDTools (Quinlan and Hall 2010); BamTools (Barnett et al. 2011); deepTools (Ramírez et al. 2016); featureCounts (Liao et al. 2014); HOMER (Heinz et al. 2010); MultiQC (Ewels et al. 2016); phamtompeakqualtools (Landt et al. 2012); preseq (Daley and Smith 2013); SAMtools (Li et al. 2009); UCSC Tools (Kent et al. 2010); DESeq2 (Love et al. 2014); Bioconda (Grüning et al. 2018); BioContainers (da Veiga Leprevost et al. 2017) and Apptainer (Kurtzer et al. 2017). The pipeline was run using hg38.p14 as reference genome from UCSC (International Human Genome Sequencing Consortium 2001) and the gene annotation from GENCODE v43

(Frankish et al. 2019). BWA was used for mapping and effective genome size for MACS2 was computed using unique-kmers.py from khmer v2.1.1 (Li and Durbin 2009; Zhang et al. 2008; Crusoe et al. 2015; Döring et al. 2008). Option --narrow_peak was specified when processing ChIP-seq datasets for CTCF and TP53.
The workflow was launched by executing script run_nfcore_chip.sh.

Calling of copy number variations

Copy number variations (CNVs) were called from Hi-C data using HiNT-CNV v2.2.8 (Wang et al. 2020).
The list of restriction sites for the Arima 2-enzyme kit was generated by running script bin/compute_restriction_sites_for_hint.py on hg38.14 (International Human Genome Sequencing Consortium 2001).
Reference data and background matrices used by HiNT were downloaded from compbio.med.harvard.edu/hint and have been archived on Zenodo at the following DOI: 10.5281/zenodo.13255302.
Data analysis steps are defined in workflow detect_structural_variants which was run by launching script run_detect_structural_variants.sh.

Annotation of structural variations

Large structural variations such as translocations were manually annotated by us by looking for square regions of enriched interactions and sharp transitions in the trans portion of the Hi-C matrix (see Supplemental Tables S15-17).

TAD analyses

We determined genomic positions of topologically associated domains (TADs) in all samples with HiCExplorer v3.7.2 using default parameters on matrices at 10, 20, 50 and 100 kbp resolutions (Ramírez et al. 2018; Wolff et al. 2018, 2020). Workflow tad_analysis.nf was used to generate the draft figures that went into Supplemental Fig. S3-6. The same workflow was also used to run HiCExplorer. Draft figures for Fig. 1A was generated using notebook bin/plotting/plot_tads_higlass.ipynb. Supplemental Fig. S5 was generated by fetching interactions at 50 kbp resolution for each 10A TAD across cell types, masking values overlapping the first 150 kbp around the diagonal. Finally interactions were summed and normalized by TAD size (as in, the number of pixels overlapping a TAD). To generate Supplemental Fig. S6, TADs from two cell types were paired based on the highest overlap (Jaccard Index of genomic coordinates), and the distribution of pairwise overlaps were plotted. TADs overlapping or around regions masked by matrix balancing were not considered, as the insulation score can be unreliable in these regions.
The analysis is encapsulated by workflow tad_analysis.nf which was run by launching script run_tad_analysis.sh.

TAD clique analyses

The TAD annotation generated by HiCExplorer was given as input to workflow github.com/robomics/call_tad_cliques v0.5.1 (doi.org/10.5281/zenodo.12689353) to identify cliques of TADs as outlined in Paulsen et al. (Paulsen et al. 2019). TAD cliques were called across all three cell types using TADs from 10A. This is a necessary simplification required to allow comparing cliques across cell types in downstream analyses. The output of github.com/robomics/call_tad_cliques was used as input for workflow

postprocess_call_tad_cliques.nf, which generated the draft version of Fig. 3B, 3C, 3D and Supplemental Figs. S31,S33-39.
Workflows were launched by running script run_call_tad_cliques_workflow.sh.

Subcompartment analyses

Subcompartments were determined using a patched version of dcHiC d4eb244 (Chakraborty et al. 2022). A and B compartment annotation was generated from subcompartments by aggregating A-subcompartments and B-subcompartments. The dcHiC processing pipeline was wrapped in workflow compartment_analysis.nf, which converts matrices in .mcool file to a format understood by dcHiC and runs all analysis steps except those for --pcatype=trans, --pcatype=fithic, --pcatype=dloop, and --pcatype=enrich. When appropriate, the reference genome assembly, annotation and .chrom.sizes for hg38.p14 were provided to dcHiC through the --gfolder option. We fixed the seed used by dcHiC to ensure our results are reproducible by others. Subcompartments were called at the following resolutions: 10 kbp, 20 kbp, 50 kbp, 100 kbp, 200 kbp and 500 kbp. However, only subcompartments at 10 kbp resolution were used for further data analyses. The same workflow was used to generate the draft figures for Fig. 1B and 1D as well as Supplemental Figs. S16-19. Fig. 1C was generated using the output of the viz step of dcHiC as the starting point.
Figure S9-11 were generated by tracking subcompartment assignments across cell types. Bins were paired based on their genomic coordinates, then subcompartment switches were classified into 5 classes: neutral (no switch), reverted (e.g. switch occurred in T1 but was reverted in C1), transition to open/close and other switches (e.g. partial reversion: A3→A1→A2). Subcompartment switches were further classified using a delta score Δ_{ij} defined as follows. We quantify the degree of switching between two stages, i and j (Δ_{ij}), by assigning ranks to the subcompartments (B3=0...A3=7) and calculating the rank difference. A negative rank difference (Δ_{ij}) thus indicates a transition towards B-type subcompartments. Conversely, a positive value signifies a shift towards A-type compartments.
Data analysis steps are defined in workflow compartment_analysis which was run by executing script run_compartment_analysis.sh.

Virtual 4C

Draft virtual 4C figures (Fig. 4D; bottom and Suppl. Fig. S48B) have been generated using notebook virtual_4c_myc.ipynb.

The two figures were generated by fetching and normalizing interactions for the following regions from the merged Hi-C maps for 10A, T1, and C1:

- Fig. 4D; bottom:
  “chr8:127736000-127737000" (MYC promoter) and
  "chr10:71280000-73310000" (10kb resolution)
- Suppl. Fig. 48B:
  “chr8:127736000-127737000" (MYC promoter) and
  “chr10:73240000-73270000” (5kb resolution)

Differential expression analyses

Differential expression analysis was performed using DESeq2 v1.38.0 and apeglm v1.20.0 (Love et al. 2014; Zhu et al. 2019).
DESeq2 was called with default parameters using the raw count table produced by nf-core/rnaseq as input. Log_2-fold-change shrinkage estimation was computed with the lfcShrink

function from DESeq2 using apeglm as shrinkage estimator and the following log2 FoldChange cutoffs: 0.0, 0.1, 0.25, 0.5, 1.0, 1.5, 2.0, 2.5, 3.0, 3.5, 4.0, 4.5, 5.0.
The analysis was automated using workflow diff_expression_analysis.nf, which was launched with run_diff_expression_analysis.sh.
Supplemental Fig. S28 was generated by running script run_cluster_profiler_do.py. The script uses clusterProfiler v4.8.1 (Wu et al. 2021; Yu et al. 2012) and the disease ontology (DO) database from the DOSE v3.26.1 package (Yu et al. 2015) to perform over-representation analysis of DO terms (Schriml et al. 2023). Package enrichplot v1.20.0 (Wu et al. 2021) was used for visualization. The IDs of differentially expressed genes were provided as input to clusterProfiler. Genes were considered as differentially expressed based if they exhibit an absolute log2FoldChange value of 0.5 or greater and a p-value of 0.01 or smaller (correcting for multiple testing). Furthermore, clusterProfiler was run using a q-value of 0.05.

Comparative analyses

All comparative analyses were performed using workflow comparative_analysis.nf.

Fig. S15 was generated by overlapping subcompartment labels with several different epigenetic markers. First, each ChIP-seq peak was assigned a score by summing the raw ChIP-seq signal over each peak, then each peak was assigned to a subcompartment. Finally peaks were grouped by subcompartment label and the mean signal was computed for each subcompartment.

Fig. 2A and Supplemental Fig. S29 were generated by overlapping expression levels in TPMs with subcompartment labels overlapping genes from GENCODE v43 for hg38. In case a gene was tagged with multiple subcompartment labels, the gene was assigned the label with the largest coverage. In case of coverage tie, the gene was discarded (note that this is an extremely rare occurrence).

Figure 2B was generated using pyGenomeTracks (Ramírez et al. 2018; Lopez-Delisle et al. 2021) to visualize up/down regulated genes overlapping a region involved in subcompartment switching.

Figures 2C-F were generated by overlapping subcompartments with differentially expressed genes across all three cell types. First genes were assigned a subcompartment label by overlapping their TSS with the subcompartment annotation generated by dcHiC. Next genes were grouped based on log2FoldChange and p-value in downregulated, non-differentially expressed and upregulated genes (lfc=2.0; pvalue=0.01). Finally each group of genes was plotted as heatmaps showing subcompartment switches across pairs of cell types (genes not involved in subcompartment switches are not shown). Figures 2D and 2F were generated from the table underlying heatmaps 2C and 2E as follows: compute the sum of genes for each diagonal i; starting from diagonal $i = 1$, pair diagonal i with diagonal $-i$; finally compute the $\log_2$ ratio between the sum of diagonal i and the sum of diagonal $-i$. Positive values indicate a positive correlation between one of the classes of differentially expressed genes and switches towards open chromatin while negative values indicate a positive correlation with subcompartment switches towards close chromatin.

The draft figure for Fig. 3A was generated with bin/plotting/plot_tad_cliques.py using TAD cliques, TADs, compartment PCA and GENCODE v43 gene annotation as input.

The draft figure for Supplemental Fig. S32 was generated by overlapping subcompartment states with TADs annotated with the size of the largest clique to which they belonged to.

The draft figures for Fig. 3F-G and Supplemental Fig. S40 were generated by clustering TADs and TAD cliques using HDBSCAN (McInnes et al. 2017; McInnes and Healy 2017) based on their subcompartment composition.

First, domains (that is TADs or TAD cliques) were annotated with their subcompartment state composition by overlapping subcompartment states with the domains using annotate_domains_with_subcompartments.py. This resulted in a count matrix with one row per domain, where each row counts the number of bins labeled for each subcompartment state. For example, given a domain overlapping 3 A1 bins, 10 A2 bins and 2 A3 bins, the entry in the count matrix corresponding to this domain would be 0, 0, 0, 0, 0, 3, 10, 2.
Next, this count matrix was given as input to cluster_domains_by_subcompartment_state.py, which clustered domains using HDBSCAN.flat based on their similarity in subcompartment composition. Clustering was performed using the following settings: n_clusters=9; metric=euclidean; min_cluster_size=200; min_samples=5; cluster_selection_method=leaf. Finally, clusters were visualized using plot_domain_subcompartment_clusters.py.

All comparative analyses are defined in workflow comparative_analysis.nf which was launched with script run_comparative_analysis.sh.

3D genome modeling

A patched version of Chrom3D v1.0.2 was used to generate 3D genome models for 10A, T1 and C1 (Paulsen et al. 2017). Briefly, this Nextflow workflow runs NCHG (doi.org/10.5281/zenodo.12680450) to identify statistically significant cis and trans interactions. Translocated regions were excluded when identifying statistically significant trans interactions. For intra-chromosomal interactions we used a log-ratio of 1.2 and adjusted-pvalue of 0.01 as cutoffs, while for inter-chromosomal interactions a log-ratio of 0.25 and adjusted-pvalue of 0.01 were used as cutoffs. The workflow then uses statistically significant interactions in Chrom3D simulations as spatially proximal interaction constraints. Furthermore, the workflow matches LADs to the corresponding TAD domains such that these domains can be used as peripheral sub-nuclear constraints in the simulations. A total of 100 Chrom3D simulations were run for each condition with a nuclear occupancy of 0.15, at TAD resolution and 2 million simulation steps (Paulsen et al. 2017).
ChimeraX was used to visualize the simulated Chrom3D models (Pettersen et al. 2021). The median distance of each chromosome from the nuclear center was calculated for each Chrom3D simulation and visualized using ggplot2 (Villanueva and Chen 2019). The median distance and the standard deviation of each subcompartment were likewise evaluated for each Chrom3D simulation and visualized using ggplot2. Subcompartment distances from the nuclear center were statistically evaluated and compared within conditions using the Wilcoxon rank sum test in R (R Core Team 2024) with the function wilcox.test.

FISH analysis

Analysis of FISH data is automated using workflow fish.nf. Draft plots have been generated using notebooks plot_fish_blob_distance_stats.ipynb and plot_fish_blob_radial_positioning.ipynb.

The FISH data analysis consists of three steps:

- Nuclei segmentation
- Probe localization
- Plot generation and statistical tests

Nuclei segmentation

Nuclei segmentation is performed using DAPI signal (i.e. the blue channel of the RGB image produced by the microscope).

First, RGB images containing one or more nuclei are converted to grayscale by extracting the blue channel from the images. Grayscale images are then sharpened using unsharp masking. This is done to improve the separation of the profiles of nuclei that are located very close to one another. Next, foreground objects (i.e. nuclei profiles) are highlighted using Otsu thresholding (Otsu 1979). Objects that are significantly smaller than plausible nuclei profiles are masked out. Next, we compute the contour of each individual object using the “marching squares” method. Finally, object contours are used to crop out individual nuclei.
To properly deal with various edge cases (such as mitotic nuclei and overlapping nuclei), nuclei whose contour significantly deviates from an ellipsoid are flagged so that they can be skipped in subsequent analysis steps. This is achieved by first fitting an ellipse to the contour detected using the first algorithm described in (Fitzgibbon and Fisher). Next, we compute the overlap coefficient (OC) between the fitted ellipse and the nucleus contour, and mask nuclei with an OC of 0.95 or lower. Finally, nuclei that are only partially visible in an image are also flagged.

Probe localization

For each nucleus, we extract the red and green channels from the RGB image produced by the segmentation step. The resulting grayscale images are processed independently as follows.
Given a probe and a cell line, we can estimate the number of probe signals we expect to find in each nucleus. This information is used to guide the blob (i.e. probe signal) detection using the Laplacian of Gaussian (LoG) method. We perform a sweep of LoG parameters, starting from parameters that are suitable to detect large blobs in an image. If the first run of the LoG algorithm detects *N* or more blobs, where *N* is the number of expected probe signals, then the parameter sweep is halted. Otherwise, the coordinates of detected blobs (if any) are stored, and the LoG algorithm is re-run using parameters to detect progressively smaller blobs. Every iteration, the coordinates of newly detected blobs are merged with the coordinates of blobs detected in previous runs of the algorithm. The parameter sweep stops as soon as *N* or more blobs are detected, or when the parameter space is exhausted.

Plot generation and statistical tests

The coordinates of blobs identified in the previous step are finally used to generate Fig. 4F and Supplemental Fig. S47.

The number of nuclei and observations for each condition is shown in Suppl. Table S18.

Color mapping strategy

We provide colorblind-friendly versions of the raw and processed FISH images. These images were generated using script color_mapping_fish.py. In brief, this script applies a local linear mapping to convert the original colors (blue for DAPI and red/green for the FISH probes) to different colors that can be more easily distinguished by those affected by common forms of colorblindness. The mapping is local because we only map colors for pixels whose original color is perceptually different from black and white.

Software used throughout data analysis code

The following software packages were used throughout the code used for data analysis:

- BEDTools (Quinlan and Hall 2010) - to perform common set operations on genomic intervals.
- bedGraphToBigWig (Kent et al. 2010) - to convert bedGraph files to bigWig format.
- bioframe (Open2C et al. 2024) to perform common set operations on genomic intervals.
- hictkpy (Rossini and Paulsen 2024) - to perform certain input-output operations on .cool files.
- Matplotlib (Hunter May-June 2007) - to generate plots.
- NumPy (Harris et al. 2020) - to efficiently perform arithmetic operations on vector data.
- OpenCV - to manipulate and process microscopy images.
- pandas (McKinney 2010) - to read, write and manipulate tabular data using dataframes.
- pyBigWig - to read and write bigWig files.
- SAMtools (Danecek et al. 2021) - to index FASTA files and perform IO operations on SAM, BAM and CRAM files.
- scikit-image (van der Walt et al. 2014) - to manipulate and process microscopy images.
- SciPy (Virtanen et al. 2020) - to compute Pearson's correlation values and perform statistical tests.
- seaborn (Waskom 2021) - to generate plots.

Software patches

This section describes the purpose of the patches we applied to Chrom3D, cooler, dcHiC, and HiNT. Patch files are available under containers/patches.

Patch for nf-core/hic v2.0.0 (https://zenodo.org/records/2669513)

Our patch involved updating the pipeline to correctly handle the --restriction_site and --ligation_site parameters.

Our patch was accepted by upstream and is now part of v2.1.0 of the pipeline. See nf-core/hic/pull/153 for more details.

Patches for dcHiC d4eb244 (Chakraborty et al. 2022)

We patched dcHiC as follows:

- Define a default seed and introduce a --seed CLI option to ensure results are reproducible across runs
- Wrap calls to depmixS4::fit into a try-catch block to attempt model fitting up to 5 times in case of spurious failures
- Properly handle the possibility that a chromosome does not have any bin overlapping one or more subcompartment type.

Our patches were accepted by upstream but are not yet part of a stable release. See ay-lab/dcHiC/pull/59, ay-lab/dcHiC/pull/60, ay-lab/dcHiC/pull/62 and containers/patches/dchic.patch for more details.

Patch for cooler v0.9.1 (Abdennur and Mirny 2020)

We patched cooler to ensure that convergence of cooler balance using cis-only interactions was correctly reported for all chromosomes instead of just the last one.

When balancing interactions using the --cis-only flag, cooler balances interactions for each chromosome independently. Given that there is no guarantee that ICE will converge within the given number of iterations, cooler balance stores an attribute inside balanced cooler files to report whether balancing was successful (i.e. convergence was achieved).
In cooler v0.9.1 there is a bug in the logic that writes this attribute that causes the convergence for the last chromosome balanced to be reported instead of the convergence status for each chromosome. Our patch addresses this bug such that the convergence status of matrices balanced with --cis-only can be assessed correctly.
The patch also addressed some minor issues related to detecting pandas' version at runtime and handling of bin sizes represented using unsigned integers.
Our patches were accepted by upstream and are now part of cooler v0.9.2.
See open2c/cooler/pull/313, open2c/cooler/pull/323, open2c/cooler/pull/324 and containers/patches/cooler.patch for more details.

Patch for Chrom3D v1.0.2 (Paulsen et al. 2017)
We patched Chrom3D to support building the project using CMake and addressing a few compiler warnings and errors that were preventing us from compiling Chrom3D with a modern C++ compiler toolchain. For more details, refer to the following two patch files available at robomics/chrom3d-nf (doi.org/10.5281/zenodo.12687842) chrom3d-cmake.patch, chrom3d-fix-warnings.patch.

Patch for HiNT v2.2.8 (Wang et al. 2020)
We patched HiNT to support processing Hi-C matrices using Arima restriction enzymes. See containers/patches/hint.patch for more details.

Data Access

All raw and processed sequencing data generated in this study have been submitted to the NCBI Gene Expression Omnibus (GEO; https://www.ncbi.nlm.nih.gov/geo/) under the following accession numbers: GSE246689, GSE246599, GSE247171, and GSE246947.
All raw and processed microscopy data generated in this study have been submitted to Zenodo (https://zenodo.org/) and are available for download at the following DOI: 10.5281/zenodo.15167335.

Competing Interests

None declared

Acknowledgments

Molecular graphics and analyses performed with UCSF ChimeraX, developed by the Resource for Biocomputing, Visualization, and Informatics at the University of California, San Francisco, with support from National Institutes of Health R01-GM129325 and the Office of Cyber Infrastructure and Computational Biology, National Institute of Allergy and Infectious Diseases. HiC and RNA-seq library constructions and Illumina sequencing were done at the Biomolecular Resource Facility (BRF), JCSMR, Australian National University. Some of the analyses were performed on resources provided by Sigma2 - the National Infrastructure for High Performance Computing and Data Storage in Norway, with account number NN8041K. We thank Anita L. Sørensen for performing FISH experiments and microscopy imaging. Lenti-multi-CRISPR was a gift from Qin Yan and hCas9 was a gift from George Church (Addgene

plasmids no. 85402 and 41815, respectively; http://n2t.net/addgene:41815 http://n2t.net/addgene:85402). This work was funded by the Norwegian Research Council project. no. 324137 (JP) and Centres of Excellence funding scheme 262652 - CanCell (RE), the Norwegian Cancer Society (PC), The Norwegian Cancer Society 272510 (RE), UNIFOR (PC and AB), and National Health and Medical Research Council ID 1182759 (DT).

Authors' contributions

JP, PC, DT conceived and designed the study; JP, RR and MO designed data analyses; RR and MO analyzed data; RR processed Hi-C, RNA-seq, ChIP-seq, and FISH data and did downstream analyses; MO performed 3D genome modeling; MN did Hi-C experiments; RD and YD did cell culture work and RNA-seq; AB and MA analyzed LADs; RE conceived and designed CRISPR-Cas9 RE strategy, verified clones, analyzed data and generated figures; ML performed cloning of Lenti-multi-CRISPR constructs and PCR; RA did CRISPR-Cas9 time-course, RNA and genomic extraction, qRT-PCR, PCR and analysis; JP, PC, DT, RE supervised the work. All authors read and approved the final manuscript.

References

Abdennur N, Mirny LA. 2020. Cooler: scalable storage for Hi-C data and other genomically labeled arrays. *Bioinformatics* **36**: 311–316.

Akdemir KC, Le VT, Chandran S, Li Y, Verhaak RG, Beroukhim R, Campbell PJ, Chin L, Dixon JR, Futreal PA, et al. 2023. Author Correction: Disruption of chromatin folding domains by somatic genomic rearrangements in human cancer. *Nat Genet* **55**: 1079.

Arnould C, Rocher V, Saur F, Bader AS, Muzzopappa F, Collins S, Lesage E, Le Bozec B, Puget N, Clouaire T, et al. 2023. Chromatin compartmentalization regulates the response to DNA damage. *Nature* **623**: 183–192.

Ay F, Noble WS. 2015. Analysis methods for studying the 3D architecture of the genome. *Genome Biol* **16**: 183.

Barnett DW, Garrison EK, Quinlan AR, Strömberg MP, Marth GT. 2011. BamTools: a C++ API and toolkit for analyzing and managing BAM files. *Bioinformatics* **27**: 1691–1692.

Barutcu AR, Lajoie BR, McCord RP, Tye CE, Hong D, Messier TL, Browne G, van Wijnen AJ, Lian JB, Stein JL, et al. 2015. Chromatin interaction analysis reveals changes in small chromosome and telomere clustering between epithelial and breast cancer cells. *Genome Biol* **16**: 214.

Berlivet S, Paquette D, Dumouchel A, Langlais D, Dostie J, Kmita M. 2013. Clustering of tissue-specific sub-TADs accompanies the regulation of HoxA genes in developing limbs. *PLoS Genet* **9**: e1004018.

Berns EMJJ, Klijn JGM, van Putten WLJ, van Staveren IL, Portengen H, Foekens JA. 1992. c-myc Amplification Is a Better Prognostic Factor than HER2/neu Amplification in Primary Breast Cancer1. *Cancer Res* **52**: 1107–1113.

Bobbitt JR, Seachrist DD, Keri RA. 2023. Chromatin Organization and Transcriptional Programming of Breast Cancer Cell Identity. *Endocrinology* **164**. http://dx.doi.org/10.1210/endocr/bqad100.

1084 Boninsegna L, Yildirim A, Polles G, Zhan Y, Quinodoz SA, Finn EH, Guttman M, Zhou XJ,
1085 Alber F. 2022. Integrative genome modeling platform reveals essentiality of rare contact
1086 events in 3D genome organizations. *Nat Methods* **19**: 938–949.

1087 Brinkman EK, Chen T, Amendola M, van Steensel B. 2014. Easy quantitative assessment of
1088 genome editing by sequence trace decomposition. *Nucleic Acids Res* **42**: e168.

1089 Bron C, Kerbosch J. 1973. Algorithm 457: finding all cliques of an undirected graph.
1090 *Communications of the ACM*. https://dl.acm.org/doi/10.1145/362342.362367 (Accessed
1091 April 10, 2025).

1092 Brunette GJ, Tourdot RW, Wangsa D, Pellman D, Zhang C-Z. 2024. Haplotype-resolved
1093 karyotype construction from Hi-C data using refLinker. *bioRxiv*.
1094 http://dx.doi.org/10.1101/2024.03.02.583108.

1095 Cao J, Wu L, Zhang S-M, Lu M, Cheung WKC, Cai W, Gale M, Xu Q, Yan Q. 2016. An easy
1096 and efficient inducible CRISPR/Cas9 platform with improved specificity for multiple gene
1097 targeting. *Nucleic Acids Res* **44**: e149.

1098 Chakraborty A, Wang JG, Ay F. 2022. dcHiC detects differential compartments across
1099 multiple Hi-C datasets. *Nat Commun* **13**: 6827.

1100 Corzo C, Corominas JM, Tusquets I, Salido M, Bellet M, Fabregat X, Serrano S, Solé F.
1101 2006. The MYC oncogene in breast cancer progression: from benign epithelium to
1102 invasive carcinoma. *Cancer Genet Cytogenet* **165**: 151–156.

1103 Cremer T, Cremer M. 2010. Chromosome territories. *Cold Spring Harb Perspect Biol* **2**:
1104 a003889.

1105 Crosetto N, Bienko M. 2020. Radial Organization in the Mammalian Nucleus. *Front Genet*
1106 **11**: 33.

1107 Crusoe MR, Alameldin HF, Awad S, Boucher E, Caldwell A, Cartwright R, Charbonneau A,
1108 Constantinides B, Edvenson G, Fay S, et al. 2015. The khmer software package:
1109 enabling efficient nucleotide sequence analysis. *F1000Res* **4**: 900.

1110 Daley T, Smith AD. 2013. Predicting the molecular complexity of sequencing libraries. *Nat*
1111 *Methods* **10**: 325–327.

1112 Danecek P, Bonfield JK, Liddle J, Marshall J, Ohan V, Pollard MO, Whitwham A, Keane T,
1113 McCarthy SA, Davies RM, et al. 2021. Twelve years of SAMtools and BCFtools.
1114 *Gigascience* **10**. http://dx.doi.org/10.1093/gigascience/giab008.

1115 da Veiga Leprevost F, Grüning BA, Alves Aflitos S, Röst HL, Uszkoreit J, Barsnes H, Vaudel
1116 M, Moreno P, Gatto L, Weber J, et al. 2017. BioContainers: an open-source and
1117 community-driven framework for software standardization. *Bioinformatics* **33**: 2580–
1118 2582.

1119 Dawson PJ, Wolman SR, Tait L, Heppner GH, Miller FR. 1996. MCF10AT: a model for the
1120 evolution of cancer from proliferative breast disease. *Am J Pathol* **148**: 313–319.

1121 Diao Y, Li B, Meng Z, Jung I, Lee AY, Dixon J, Maliskova L, Guan K-L, Shen Y, Ren B.
1122 2016. A new class of temporarily phenotypic enhancers identified by CRISPR/Cas9-
1123 mediated genetic screening. *Genome Res* **26**: 397–405.

1124 Di Tommaso P, Chatzou M, Floden EW, Barja PP, Palumbo E, Notredame C. 2017.
1125 Nextflow enables reproducible computational workflows. *Nat Biotechnol* **35**: 316–319.

1126 Dixon JR, Jung I, Selvaraj S, Shen Y, Antosiewicz-Bourget JE, Lee AY, Ye Z, Kim A,
1127 Rajagopal N, Xie W, et al. 2015. Chromatin architecture reorganization during stem cell
1128 differentiation. *Nature* **518**: 331–336.

1129 Dixon JR, Selvaraj S, Yue F, Kim A, Li Y, Shen Y, Hu M, Liu JS, Ren B. 2012. Topological
1130 domains in mammalian genomes identified by analysis of chromatin interactions. *Nature*
1131 **485**: 376–380.

1132 Dobin A, Davis CA, Schlesinger F, Drenkow J, Zaleski C, Jha S, Batut P, Chaisson M,
1133 Gingeras TR. 2013. STAR: ultrafast universal RNA-seq aligner. *Bioinformatics* **29**: 15–
1134 21.

1135 Döring A, Weese D, Rausch T, Reinert K. 2008. SeqAn an efficient, generic C++ library for
1136 sequence analysis. *BMC Bioinformatics* **9**: 11.

1137 Dozmorov MG, Marshall MA, Rashid NS, Grible JM, Valentine A, Olex AL, Murthy K,
1138 Chakraborty A, Reyna J, Figueroa DS, et al. 2023. Publisher Correction: Rewiring of the
1139 3D genome during acquisition of carboplatin resistance in a triple-negative breast
1140 cancer patient-derived xenograft. *Sci Rep* **13**: 7522.

1141 Durand NC, Shamim MS, Machol I, Rao SSP, Huntley MH, Lander ES, Aiden EL. 2016.
1142 Juicer Provides a One-Click System for Analyzing Loop-Resolution Hi-C Experiments.
1143 *Cell Syst* **3**: 95–98.

1144 Ewels PA, Peltzer A, Fillinger S, Patel H, Alneberg J, Wilm A, Garcia MU, Di Tommaso P,
1145 Nahnsen S. 2020. The nf-core framework for community-curated bioinformatics
1146 pipelines. *Nat Biotechnol* **38**: 276–278.

1147 Ewels P, Magnusson M, Lundin S, Käller M. 2016. MultiQC: summarize analysis results for
1148 multiple tools and samples in a single report. *Bioinformatics* **32**: 3047–3048.

1149 Feng Y, Pauklin S. 2020. Revisiting 3D chromatin architecture in cancer development and
1150 progression. *Nucleic Acids Res* **48**: 10632–10647.

1151 Fitzgibbon A, Fisher RB. A Buyer's Guide to Conic Fitting.
1152 http://www.bmva.org/bmvc/1995/bmvc-95-050.html.

1153 Forsberg F, Brunet A, Ali TML, Collas P. 2019. Interplay of lamin A and lamin B LADs on the
1154 radial positioning of chromatin. *Nucleus* **10**: 7–20.

1155 Frankish A, Diekhans M, Ferreira A-M, Johnson R, Jungreis I, Loveland J, Mudge JM, Sisu
1156 C, Wright J, Armstrong J, et al. 2019. GENCODE reference annotation for the human
1157 and mouse genomes. *Nucleic Acids Res* **47**: D766–D773.

1158 Gao T, Qian J. 2020. EnhancerAtlas 2.0: an updated resource with enhancer annotation in
1159 586 tissue/cell types across nine species. *Nucleic Acids Res* **48**: D58–D64.

1160 Garg S. 2023. Towards routine chromosome-scale haplotype-resolved reconstruction in
1161 cancer genomics. *Nat Commun* **14**: 1358.

1162 Gonzalez-Sandoval A, Gasser SM. 2016. On TADs and LADs: Spatial Control Over Gene
1163 Expression. *Trends Genet* **32**: 485–495.

1164 Grisanzio C, Freedman ML. 2010. Chromosome 8q24-Associated Cancers and MYC. *Genes*
1165 *Cancer* **1**: 555–559.

1166 Grüning B, Dale R, Sjödin A, Chapman BA, Rowe J, Tomkins-Tinch CH, Valieris R, Köster J,

Bioconda Team. 2018. Bioconda: sustainable and comprehensive software distribution for the life sciences. *Nat Methods* **15**: 475–476.

Haeussler M, Schönig K, Eckert H, Eschstruth A, Mianné J, Renaud J-B, Schneider-Maunoury S, Shkumatava A, Teboul L, Kent J, et al. 2016. Evaluation of off-target and on-target scoring algorithms and integration into the guide RNA selection tool CRISPOR. *Genome Biol* **17**: 148.

Harris CR, Millman KJ, van der Walt SJ, Gommers R, Virtanen P, Cournapeau D, Wieser E, Taylor J, Berg S, Smith NJ, et al. 2020. Array programming with NumPy. *Nature* **585**: 357–362.

Harris HL, Gu H, Olshansky M, Wang A, Farabella I, Eliaz Y, Kalluchi A, Krishna A, Jacobs M, Cauer G, et al. 2023. Chromatin alternates between A and B compartments at kilobase scale for subgenic organization. *Nat Commun* **14**: 3303.

Heinz S, Benner C, Spann N, Bertolino E, Lin YC, Laslo P, Cheng JX, Murre C, Singh H, Glass CK. 2010. Simple combinations of lineage-determining transcription factors prime cis-regulatory elements required for macrophage and B cell identities. *Mol Cell* **38**: 576–589.

Hoff DDV, Needham-VanDevanter DR, Yucel J, Windle BE, Wahl GM. 1988. Amplified human MYC oncogenes localized to replicating submicroscopic circular DNA molecules. *Proceedings of the National Academy of Sciences* **85**: 4804–4808.

Hsieh T-HS, Cattoglio C, Slobodyanyuk E, Hansen AS, Rando OJ, Tjian R, Darzacq X. 2020. Resolving the 3D landscape of transcription-linked mammalian chromatin folding. *Mol Cell* **78**: 539–553.e8.

Hung KL, Luebeck J, Dehkordi SR, Colón CI, Li R, Wong IT-L, Coruh C, Dharanipragada P, Lomeli SH, Weiser NE, et al. 2022. Targeted profiling of human extrachromosomal DNA by CRISPR-CATCH. *Nat Genet* **54**: 1746–1754.

Hung KL, Yost KE, Xie L, Shi Q, Helmsauer K, Luebeck J, Schöpflin R, Lange JT, Chamorro González R, Weiser NE, et al. 2021. ecDNA hubs drive cooperative intermolecular oncogene expression. *Nature* **600**: 731–736.

Hunter JD. May-June 2007. Matplotlib: A 2D Graphics Environment. *Comput Sci Eng* **9**: 90–95.

Ibrahim DM, Mundlos S. 2020. Three-dimensional chromatin in disease: What holds us together and what drives us apart? *Curr Opin Cell Biol* **64**: 1–9.

International Human Genome Sequencing Consortium. 2001. Initial sequencing and analysis of the human genome. *Nature* **409**: 860–921.

Johnstone SE, Reyes A, Qi Y, Adriaens C, Hegazi E, Pelka K, Chen JH, Zou LS, Drier Y, Hecht V, et al. 2020. Large-Scale Topological Changes Restrain Malignant Progression in Colorectal Cancer. *Cell* **182**: 1474–1489.e23.

Kent WJ, Zweig AS, Barber G, Hinrichs AS, Karolchik D. 2010. BigWig and BigBed: enabling browsing of large distributed datasets. *Bioinformatics* **26**: 2204–2207.

Kim T, Han S, Chun Y, Yang H, Min H, Jeon SY, Kim J-I, Moon H-G, Lee D. 2022. Comparative characterization of 3D chromatin organization in triple-negative breast cancers. *Exp Mol Med* **54**: 585–600.

1209 Kopylova E, Noé L, Touzet H. 2012. SortMeRNA: fast and accurate filtering of ribosomal
1210 RNAs in metatranscriptomic data. *Bioinformatics* **28**: 3211–3217.

1211 Kovaka S, Zimin AV, Pertea GM, Razaghi R, Salzberg SL, Pertea M. 2019. Transcriptome
1212 assembly from long-read RNA-seq alignments with StringTie2. *Genome Biol* **20**: 278.

1213 Kurtzer GM, Sochat V, Bauer MW. 2017. Singularity: Scientific containers for mobility of
1214 compute. *PLoS One* **12**: e0177459.

1215 Lajoie BR, Dekker J, Kaplan N. 2015. The Hitchhiker's guide to Hi-C analysis: practical
1216 guidelines. *Methods* **72**: 65–75.

1217 Landt SG, Marinov GK, Kundaje A, Kheradpour P, Pauli F, Batzoglou S, Bernstein BE,
1218 Bickel P, Brown JB, Cayting P, et al. 2012. ChIP-seq guidelines and practices of the
1219 ENCODE and modENCODE consortia. *Genome Res* **22**: 1813–1831.

1220 Langmead B, Salzberg SL. 2012. Fast gapped-read alignment with Bowtie 2. *Nat Methods* **9**:
1221 357–359.

1222 Lee EYHP, Muller WJ. 2010. Oncogenes and tumor suppressor genes. *Cold Spring Harb*
1223 *Perspect Biol* **2**: a003236.

1224 Liao DJ, Dickson RB. 2000. c-Myc in breast cancer. *Endocr Relat Cancer* **7**: 143–164.

1225 Liao Y, Smyth GK, Shi W. 2014. featureCounts: an efficient general purpose program for
1226 assigning sequence reads to genomic features. *Bioinformatics* **30**: 923–930.

1227 Lieberman-Aiden E, van Berkum NL, Williams L, Imakaev M, Ragoczy T, Telling A, Amit I,
1228 Lajoie BR, Sabo PJ, Dorschner MO, et al. 2009. Comprehensive mapping of long-range
1229 interactions reveals folding principles of the human genome. *Science* **326**: 289–293.

1230 Li H, Durbin R. 2009. Fast and accurate short read alignment with Burrows-Wheeler
1231 transform. *Bioinformatics* **25**: 1754–1760.

1232 Li H, Handsaker B, Wysoker A, Fennell T, Ruan J, Homer N, Marth G, Abecasis G, Durbin
1233 R, 1000 Genome Project Data Processing Subgroup. 2009. The Sequence
1234 Alignment/Map format and SAMtools. *Bioinformatics* **25**: 2078–2079.

1235 Lin D, Sanders J, Noble WS. 2021. HiCRep.py: fast comparison of Hi-C contact matrices in
1236 Python. *Bioinformatics* **37**: 2996–2997.

1237 Li Q, Tjong H, Li X, Gong K, Zhou XJ, Chiolo I, Alber F. 2017. The three-dimensional
1238 genome organization of Drosophila melanogaster through data integration. *Genome Biol*
1239 **18**: 145.

1240 Liu Y, Nanni L, Sungalee S, Zufferey M, Tavernari D, Mina M, Ceri S, Oricchio E, Ciriello G.
1241 2021. Systematic inference and comparison of multi-scale chromatin sub-compartments
1242 connects spatial organization to cell phenotypes. *Nat Commun* **12**: 2439.

1243 Li Y, Xu W, Wang Y, Kou J, Zhang J, Hu S, Zhang L, Wang J, Liu J, Liu H, et al. 2022. An
1244 improved, chromosome-level genome of the giant panda (Ailuropoda melanoleuca).
1245 *Genomics* **114**: 110501.

1246 Lopez-Delisle L, Rabbani L, Wolff J, Bhardwaj V, Backofen R, Grüning B, Ramírez F, Manke
1247 T. 2021. pyGenomeTracks: reproducible plots for multivariate genomic datasets.
1248 *Bioinformatics* **37**: 422–423.

1249 Love MI, Huber W, Anders S. 2014. Moderated estimation of fold change and dispersion for
1250 RNA-seq data with DESeq2. *Genome Biol* **15**: 550.

1251 Love MI, Soneson C, Hickey PF, Johnson LK, Pierce NT, Shepherd L, Morgan M, Patro R.
1252 2020. Tximeta: Reference sequence checksums for provenance identification in RNA-
1253 seq. *PLoS Comput Biol* **16**: e1007664.

1254 Lund E, Oldenburg AR, Collas P. 2014. Enriched domain detector: a program for detection
1255 of wide genomic enrichment domains robust against local variations. *Nucleic Acids Res*
1256 **42**: e92.

1257 Mali P, Yang L, Esvelt KM, Aach J, Guell M, DiCarlo JE, Norville JE, Church GM. 2013.
1258 RNA-guided human genome engineering via Cas9. *Science* **339**: 823–826.

1259 McInnes L, Healy J. 2017. Accelerated Hierarchical Density Based Clustering. In *2017 IEEE*
1260 *International Conference on Data Mining Workshops (ICDMW)*, pp. 33–42, IEEE.

1261 McInnes L, Healy J, Astels S. 2017. hdbscan: Hierarchical density based clustering. *J Open*
1262 *Source Softw* **2**: 205.

1263 McKinney W. 2010. Data Structures for Statistical Computing in Python. In *Proceedings of*
1264 *the 9th Python in Science Conference*, SciPy
1265 https://conference.scipy.org/proceedings/scipy2010/pdfs/mckinney.pdf (Accessed
1266 November 8, 2023).

1267 Misteli T. 2004. Spatial positioning; a new dimension in genome function. *Cell* **119**: 153–156.

1268 Morton AR, Dogan-Artun N, Faber ZJ, MacLeod G, Bartels CF, Piazza MS, Allan KC, Mack
1269 SC, Wang X, Gimple RC, et al. 2019. Functional Enhancers Shape Extrachromosomal
1270 Oncogene Amplifications. *Cell* **179**: 1330–1341.e13.

1271 Nagai LAE, Park S-J, Nakai K. 2019. Analyzing the 3D chromatin organization coordinating
1272 with gene expression regulation in B-cell lymphoma. *BMC Med Genomics* **11**: 127.

1273 Nora EP, Goloborodko A, Valton A-L, Gibcus JH, Uebersohn A, Abdennur N, Dekker J,
1274 Mirny LA, Bruneau BG. 2017. Targeted Degradation of CTCF Decouples Local
1275 Insulation of Chromosome Domains from Genomic Compartmentalization. *Cell* **169**:
1276 930–944.e22.

1277 Nora EP, Lajoie BR, Schulz EG, Giorgetti L, Okamoto I, Servant N, Piolot T, van Berkum NL,
1278 Meisig J, Sedat J, et al. 2012. Spatial partitioning of the regulatory landscape of the X-
1279 inactivation centre. *Nature* **485**: 381–385.

1280 Okonechnikov K, Conesa A, García-Alcalde F. 2016. Qualimap 2: advanced multi-sample
1281 quality control for high-throughput sequencing data. *Bioinformatics* **32**: 292–294.

1282 Open2C, Abdennur N, Fudenberg G, Flyamer I, Galitsyna AA, Goloborodko A, Imakaev M,
1283 Venev SV. 2024. Bioframe: operations on genomic intervals in Pandas dataframes.
1284 *Bioinformatics* **40**: btae088.

1285 Osborne CS, Chakalova L, Mitchell JA, Horton A, Wood AL, Bolland DJ, Corcoran AE,
1286 Fraser P. 2007. Myc dynamically and preferentially relocates to a transcription factory
1287 occupied by Igh. *PLoS Biol* **5**: e192.

1288 Osman N, Shawky A-E-M, Brylinski M. 2022. Exploring the effects of genetic variation on
1289 gene regulation in cancer in the context of 3D genome structure. *BMC Genom Data* **23**:
1290 13.

1291 Osterwalder M, Barozzi I, Tissières V, Fukuda-Yuzawa Y, Mannion BJ, Afzal SY, Lee EA,
1292 Zhu Y, Plajzer-Frick I, Pickle CS, et al. 2018. Enhancer redundancy provides phenotypic
1293 robustness in mammalian development. *Nature* **554**: 239–243.

1294 Otsu N. 1979. A Threshold Selection Method from Gray-Level Histograms. *IEEE Trans Syst*
1295 *Man Cybern* **9**: 62–66.

1296 Park DS, Nguyen SC, Isenhart R, Shah PP, Kim W, Barnett RJ, Chandra A, Luppino JM,
1297 Harke J, Wai M, et al. 2023. High-throughput Oligopaint screen identifies druggable 3D
1298 genome regulators. *Nature* **620**: 209–217.

1299 Patro R, Duggal G, Love MI, Irizarry RA, Kingsford C. 2017. Salmon provides fast and bias-
1300 aware quantification of transcript expression. *Nat Methods* **14**: 417–419.

1301 Paulsen J, Liyakat Ali TM, Collas P. 2018. Computational 3D genome modeling using
1302 Chrom3D. *Nat Protoc* **13**: 1137–1152.

1303 Paulsen J, Liyakat Ali TM, Nekrasov M, Delbarre E, Baudement M-O, Kurscheid S,
1304 Tremethick D, Collas P. 2019. Long-range interactions between topologically
1305 associating domains shape the four-dimensional genome during differentiation. *Nat*
1306 *Genet* **51**: 835–843.

1307 Paulsen J, Sekelja M, Oldenburg AR, Barateau A, Briand N, Delbarre E, Shah A, Sørensen
1308 AL, Vigouroux C, Buendia B, et al. 2017. Chrom3D: three-dimensional genome
1309 modeling from Hi-C and nuclear lamin-genome contacts. *Genome Biol* **18**: 21.

1310 Pei L, Huang X, Liu Z, Tian X, You J, Li J, Fang DD, Lindsey K, Zhu L, Zhang X, et al. 2022.
1311 Dynamic 3D genome architecture of cotton fiber reveals subgenome-coordinated
1312 chromatin topology for 4-staged single-cell differentiation. *Genome Biol* **23**: 45.

1313 Perez G, Barber GP, Benet-Pages A, Casper J, Clawson H, Diekhans M, Fischer C,
1314 Gonzalez JN, Hinrichs AS, Lee CM, et al. 2025. The UCSC Genome Browser database:
1315 2025 update. *Nucleic Acids Res* **53**: D1243–D1249.

1316 Pertea G, Pertea M. 2020. GFF Utilities: GffRead and GffCompare. *F1000Res* **9**.
1317 http://dx.doi.org/10.12688/f1000research.23297.2.

1318 Pettersen EF, Goddard TD, Huang CC, Meng EC, Couch GS, Croll TI, Morris JH, Ferrin TE.
1319 2021. UCSF ChimeraX: Structure visualization for researchers, educators, and
1320 developers. *Protein Sci* **30**: 70–82.

1321 Pfaffl MW. 2001. A new mathematical model for relative quantification in real-time RT-PCR.
1322 *Nucleic Acids Res* **29**: e45.

1323 Quinlan AR, Hall IM. 2010. BEDTools: a flexible suite of utilities for comparing genomic
1324 features. *Bioinformatics* **26**: 841–842.

1325 Ramírez F, Bhardwaj V, Arrigoni L, Lam KC, Grüning BA, Villaveces J, Habermann B,
1326 Akhtar A, Manke T. 2018. High-resolution TADs reveal DNA sequences underlying
1327 genome organization in flies. *Nat Commun* **9**: 189.

1328 Ramírez F, Ryan DP, Grüning B, Bhardwaj V, Kilpert F, Richter AS, Heyne S, Dündar F,
1329 Manke T. 2016. deepTools2: a next generation web server for deep-sequencing data
1330 analysis. *Nucleic Acids Res* **44**: W160–5.

1331 Rao SSP, Huang S-C, Glenn St Hilaire B, Engreitz JM, Perez EM, Kieffer-Kwon K-R,
1332 Sanborn AL, Johnstone SE, Bascom GD, Bochkov ID, et al. 2017. Cohesin Loss

1333 Eliminates All Loop Domains. *Cell* **171**: 305–320.e24.

1334 Rao SSP, Huntley MH, Durand NC, Stamenova EK, Bochkov ID, Robinson JT, Sanborn AL,
1335 Machol I, Omer AD, Lander ES, et al. 2014. A 3D map of the human genome at
1336 kilobase resolution reveals principles of chromatin looping. *Cell* **159**: 1665–1680.

1337 Rasmussen R. 2001. Quantification on the LightCycler. In *Rapid Cycle Real-Time PCR*, pp.
1338 21–34, Springer Berlin Heidelberg, Berlin, Heidelberg.

1339 R Core Team. 2024. R: A Language and Environment for Statistical Computing.
1340 https://www.R-project.org.

1341 Rønningen T, Shah A, Oldenburg AR, Vekterud K, Delbarre E, Moskaug JØ, Collas P. 2015.
1342 Prepatterning of differentiation-driven nuclear lamin A/C-associated chromatin domains
1343 by GlcNAcylated histone H2B. *Genome Res* **25**: 1825–1835.

1344 Rossini R, Paulsen J. 2024. hictk: blazing fast toolkit to work with .hic and .cool files.
1345 *Bioinformatics* **40**. http://dx.doi.org/10.1093/bioinformatics/btae408.

1346 Rowley MJ, Corces VG. 2018. Organizational principles of 3D genome architecture. *Nat Rev*
1347 *Genet* **19**: 789–800.

1348 Santner SJ, Dawson PJ, Tait L, Soule HD, Eliason J, Mohamed AN, Wolman SR, Heppner
1349 GH, Miller FR. 2001. Malignant MCF10CA1 cell lines derived from premalignant human
1350 breast epithelial MCF10AT cells. *Breast Cancer Res Treat* **65**: 101–110.

1351 Sayols S, Scherzinger D, Klein H. 2016. dupRadar: a Bioconductor package for the
1352 assessment of PCR artifacts in RNA-Seq data. *BMC Bioinformatics* **17**: 428.

1353 Schriml LM, Lichenstein R, Bisordi K, Bearer C, Baron JA, Greene C. 2023. Modeling the
1354 enigma of complex disease etiology. *J Transl Med* **21**: 148.

1355 Schwarzer W, Abdennur N, Goloborodko A, Pekowska A, Fudenberg G, Loe-Mie Y,
1356 Fonseca NA, Huber W, Haering CH, Mirny L, et al. 2017. Two independent modes of
1357 chromatin organization revealed by cohesin removal. *Nature* **551**: 51–56.

1358 Servant N, Varoquaux N, Heard E, Barillot E, Vert J-P. 2018. Effective normalization for copy
1359 number variation in Hi-C data. *BMC Bioinformatics* **19**: 313.

1360 Servant N, Varoquaux N, Lajoie BR, Viara E, Chen C-J, Vert J-P, Heard E, Dekker J, Barillot
1361 E. 2015. HiC-Pro: an optimized and flexible pipeline for Hi-C data processing. *Genome*
1362 *Biol* **16**: 259.

1363 Sexton T, Yaffe E, Kenigsberg E, Bantignies F, Leblanc B, Hoichman M, Parrinello H, Tanay
1364 A, Cavalli G. 2012. Three-dimensional folding and functional organization principles of
1365 the Drosophila genome. *Cell* **148**: 458–472.

1366 Shen W, Le S, Li Y, Hu F. 2016. SeqKit: A Cross-Platform and Ultrafast Toolkit for FASTA/Q
1367 File Manipulation. *PLoS One* **11**: e0163962.

1368 Sood V, Misteli T. 2022. The stochastic nature of genome organization and function. *Curr*
1369 *Opin Genet Dev* **72**: 45–52.

1370 Sørlie T, Perou CM, Tibshirani R, Aas T, Geisler S, Johnsen H, Hastie T, Eisen MB, van de
1371 Rijn M, Jeffrey SS, et al. 2001. Gene expression patterns of breast carcinomas
1372 distinguish tumor subclasses with clinical implications. *Proc Natl Acad Sci U S A* **98**:
1373 10869–10874.

1374 Splinter E, de Wit E, van de Werken HJG, Klous P, de Laat W. 2012. Determining long-
1375 range chromatin interactions for selected genomic sites using 4C-seq technology: from
1376 fixation to computation. *Methods* **58**: 221–230.

1377 Spracklin G, Abdennur N, Imakaev M, Chowdhury N, Pradhan S, Mirny LA, Dekker J. 2023.
1378 Diverse silent chromatin states modulate genome compartmentalization and loop
1379 extrusion barriers. *Nat Struct Mol Biol* **30**: 38–51.

1380 van der Walt S, Schönberger JL, Nunez-Iglesias J, Boulogne F, Warner JD, Yager N,
1381 Gouillart E, Yu T, scikit-image contributors. 2014. scikit-image: image processing in
1382 Python. *PeerJ* **2**: e453.

1383 van Steensel B, Belmont AS. 2017. Lamina-Associated Domains: Links with Chromosome
1384 Architecture, Heterochromatin, and Gene Repression. *Cell* **169**: 780–791.

1385 Vilarrasa-Blasi R, Soler-Vila P, Verdaguer-Dot N, Russiñol N, Di Stefano M, Chapaprieta V,
1386 Clot G, Farabella I, Cuscó P, Kulis M, et al. 2021. Dynamics of genome architecture and
1387 chromatin function during human B cell differentiation and neoplastic transformation.
1388 *Nat Commun* **12**: 651.

1389 Villanueva RAM, Chen ZJ. 2019. ggplot2: Elegant Graphics for Data Analysis (2nd ed.).
1390 *Measurement* **17**: 160–167.

1391 Virtanen P, Gommers R, Oliphant TE, Haberland M, Reddy T, Cournapeau D, Burovski E,
1392 Peterson P, Weckesser W, Bright J, et al. 2020. SciPy 1.0: fundamental algorithms for
1393 scientific computing in Python. *Nat Methods* **17**: 261–272.

1394 Visscher DW, Wallis T, Awussah S, Mohamed A, Crissman JD. 1997. Evaluation of MYC
1395 and chromosome 8 copy number in breast carcinoma by interphase cytogenetics.
1396 *Genes Chromosomes Cancer* **18**: 1–7.

1397 Wang L, Wang S, Li W. 2012. RSeQC: quality control of RNA-seq experiments.
1398 *Bioinformatics* **28**: 2184–2185.

1399 Wang S, Lee S, Chu C, Jain D, Kerpedjiev P, Nelson GM, Walsh JM, Alver BH, Park PJ.
1400 2020. HiNT: a computational method for detecting copy number variations and
1401 translocations from Hi-C data. *Genome Biol* **21**: 73.

1402 Wang X, Xu J, Zhang B, Hou Y, Song F, Lyu H, Yue F. 2021. Genome-wide detection of
1403 enhancer-hijacking events from chromatin interaction data in rearranged genomes. *Nat*
1404 *Methods* **18**: 661–668.

1405 Wang X, Yan J, Ye Z, Zhang Z, Wang S, Hao S, Shen B, Wei G. 2022. Reorganization of 3D
1406 chromatin architecture in doxorubicin-resistant breast cancer cells. *Front Cell Dev Biol*
1407 **10**: 974750.

1408 Waskom M. 2021. seaborn: statistical data visualization. *J Open Source Softw* **6**: 3021.

1409 Wolff J, Bhardwaj V, Nothjunge S, Richard G, Renschler G, Gilsbach R, Manke T, Backofen
1410 R, Ramírez F, Grüning BA. 2018. Galaxy HiCExplorer: a web server for reproducible Hi-
1411 C data analysis, quality control and visualization. *Nucleic Acids Res* **46**: W11–W16.

1412 Wolff J, Rabbani L, Gilsbach R, Richard G, Manke T, Backofen R, Grüning BA. 2020. Galaxy
1413 HiCExplorer 3: a web server for reproducible Hi-C, capture Hi-C and single-cell Hi-C
1414 data analysis, quality control and visualization. *Nucleic Acids Res* **48**: W177–W184.

1415 Wu T, Hu E, Xu S, Chen M, Guo P, Dai Z, Feng T, Zhou L, Tang W, Zhan L, et al. 2021.

clusterProfiler 4.0: A universal enrichment tool for interpreting omics data. *Innovation (Camb)* **2**: 100141.

Yang T, Zhang F, Yardımcı GG, Song F, Hardison RC, Noble WS, Yue F, Li Q. 2017. HiCRep: assessing the reproducibility of Hi-C data using a stratum-adjusted correlation coefficient. *Genome Res* **27**: 1939–1949.

Yu G, Wang L-G, Han Y, He Q-Y. 2012. clusterProfiler: an R package for comparing biological themes among gene clusters. *OMICS* **16**: 284–287.

Yu G, Wang L-G, Yan G-R, He Q-Y. 2015. DOSE: an R/Bioconductor package for disease ontology semantic and enrichment analysis. *Bioinformatics* **31**: 608–609.

Zhang Y, Liu T, Meyer CA, Eeckhoute J, Johnson DS, Bernstein BE, Nusbaum C, Myers RM, Brown M, Li W, et al. 2008. Model-based analysis of ChIP-Seq (MACS). *Genome Biol* **9**: R137.

Zhao Y, Ding Y, He L, Zhou Q, Chen X, Li Y, Alfonsi MV, Wu Z, Sun H, Wang H. 2023. Multiscale 3D genome reorganization during skeletal muscle stem cell lineage progression and aging. *Sci Adv* **9**: eabo1360.

Zhou Y, Gerrard DL, Wang J, Li T, Yang Y, Fritz AJ, Rajendran M, Fu X, Stein G, Schiff R, et al. 2019. Temporal dynamic reorganization of 3D chromatin architecture in hormone-induced breast cancer and endocrine resistance. *Nat Commun* **10**: 1522.

Zhu A, Ibrahim JG, Love MI. 2019. Heavy-tailed prior distributions for sequence count data: removing the noise and preserving large differences. *Bioinformatics* **35**: 2084–2092.

Zhu Q, Zhao X, Zhang Y, Li Y, Liu S, Han J, Sun Z, Wang C, Deng D, Wang S, et al. 2023. Single cell multi-omics reveal intra-cell-line heterogeneity across human cancer cell lines. *Nat Commun* **14**: 8170.

1452 **Figures**

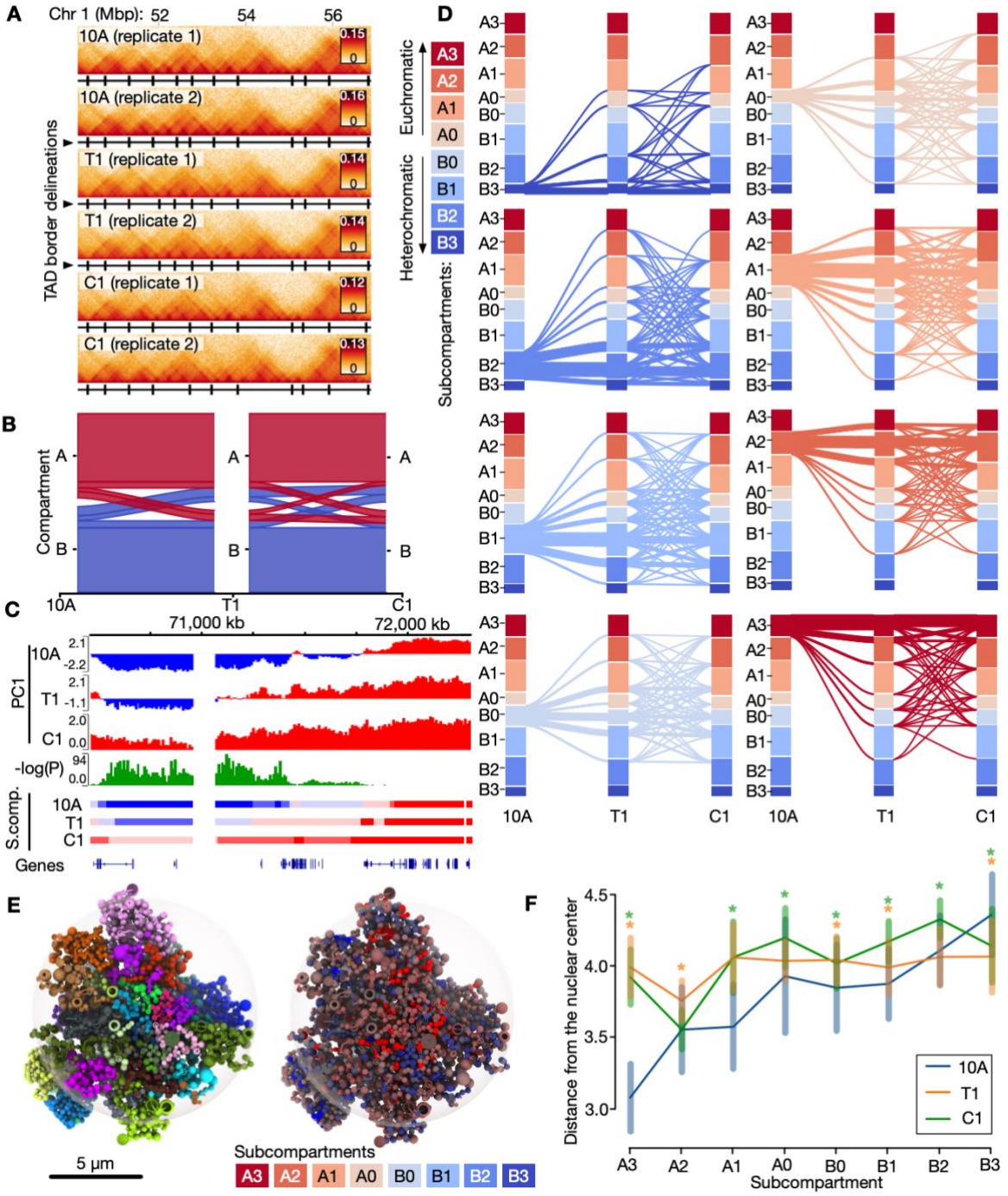

Fig. 1. Alterations in genome compartment properties during breast cancer progression stages. **A:** Example Hi-C data for a region on Chromosome 1. TAD delineations are shown as black vertical lines below each track. **B**: Alluvial plot showing A/B compartment conservation and switching during progression from 10A (left), via T1 (middle) and to C1 (right). **C**: Example region on Chromosome 11 showing a statistically significant switch in the first principal component (PC1) in the three stages. Corresponding subcompartments in the three stages (10A, T1, C1) are shown below. **D**: Switching between four A-type subcompartments (A0-A3), and four B-type (B0-B3) called from the Hi-C data (shown in distinct colors). Subcompartment switches across 10A, T1 and C1 shown as separate alluvial plots starting at each of the eight different subcompartments in 10A. **E**: Left: Tomographic view of exemplary Chrom3D model from 10A cells with chromosomes colored individually. Right: The same model with regions colored by their subcompartment associations. **F**: Median distance (with standard deviation) from the nuclear center for each subcompartment in each condition. Asterisks indicate significant differences in T1 and C1 compared to 10A (see Supplemental Table S4)

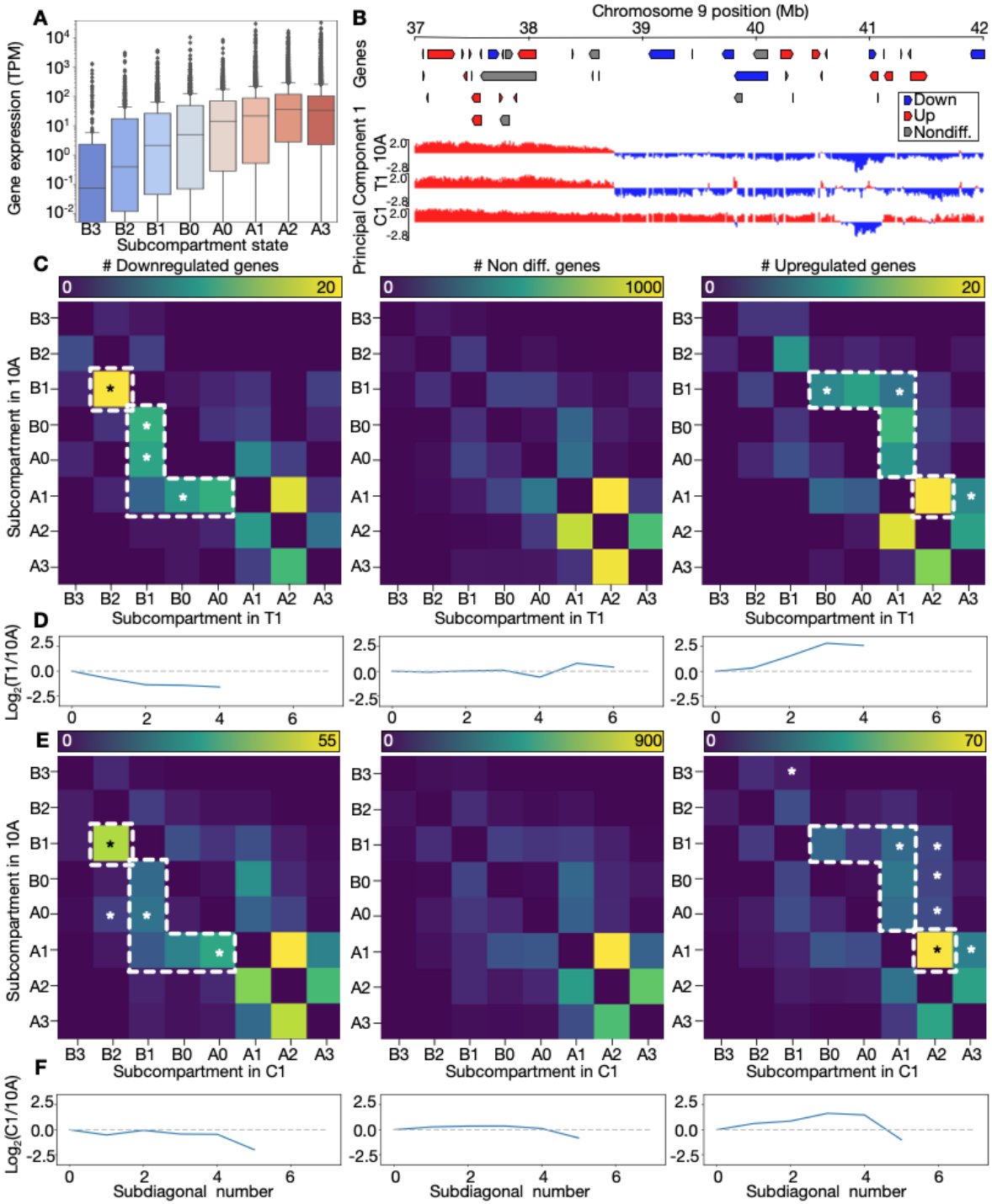

Fig. 2. Coordinated changes in subcompartments and gene expression. **A**: Gene expression levels (TPM) by subcompartment state (protein-coding genes; MCF10A [replicates merged]). Vertical axis in log scale. **B**: Example of subcompartment switching on Chromosome 9. Up- and downregulated genes in C1 vs. 10A indicated in red and blue, respectively. **C**: Heatmaps showing number of DE downregulated genes (left panel), non-differential genes (middle panel) and upregulated genes (right panel) in subcompartments switching between 10A (vertical axis) and T1 (horizontal axis). Dotted lines highlight regions with enrichment relative to non-differential and upregulated genes. Asterisks indicate significant differences (see Suppl. Table S6) **D**: Log_2-ratio of number of genes in subdiagonal sums in the upper vs. lower triangular of the corresponding heatmap from C. Ratio not displayed for subdiagonal sums that are equal to zero. **E**: Heatmaps as in C but contrasting 10A with C1. Dotted lines highlight regions with enrichment relative to non-differential and downregulated genes. Asterisks indicate significant differences (see Suppl. Table S7) **F**: Log_2-ratio plots as in D, but contrasting 10A with C1.

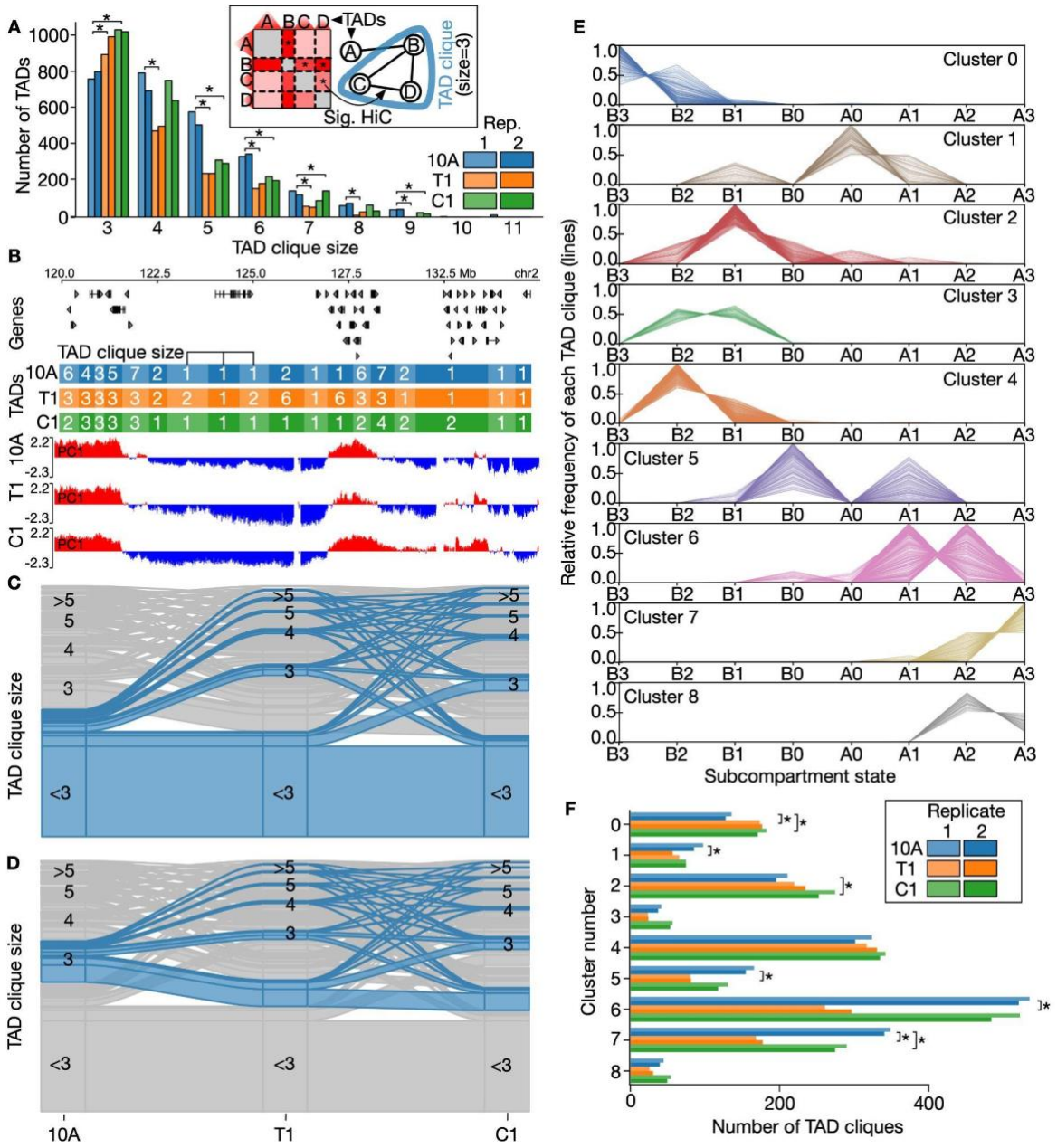

Fig. 3. TAD clique dynamics during breast cancer progression stages. **A**: Absolute number of TADs in cliques with maximal size ranging from 3 to 11 shown for each of the three breast cancer stages. Asterisks indicate significant differences (see Suppl. Table S10). Inset illustrates how "TAD cliques" are identified from the statistically significant HiC-interactions between TADs. **B**: Example region on Chromosome 2 showing changes in TAD clique sizes and compartment eigenvalues. **C**: Alluvial plots highlighting the alluvial path of a non-clique in 10A across the three cancer stages. **D**: Alluvial path of a TAD clique of size 3 in 10A. **E**: TAD clique clustering into 9 clusters based on their enrichment in subcompartments in the same cell type (vertical axis). Each line represents a TAD clique. **F**: Numbers of TAD cliques belonging to each of the clusters in E. Asterisks indicate significant differences (see Suppl. Table S12). See Suppl. Fig. S40 for numbers in the "mixed" cluster.

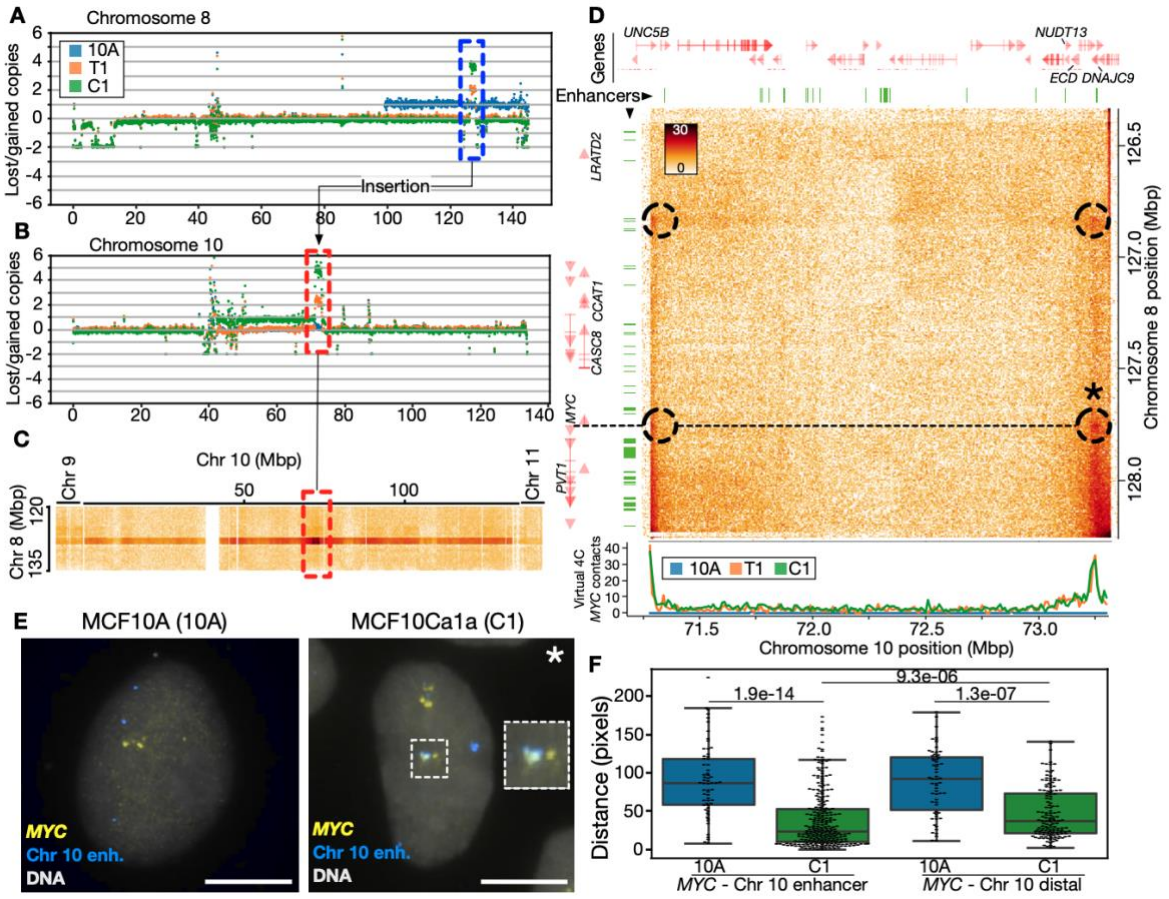

Fig. 4. *MYC* locus insertion on Chromosome 10 is accompanied by *de novo* contacts with a potential enhancer element. **A**: Lost and gained copies for the entire Chromosome 8 in 10A, T1, and C1 cells. The dotted blue box highlights specific amplification of the Chromosome 10 region. **B**: Lost and gained copies for the entire Chromosome 10, with a dotted red box highlighting specific amplifications. **C**: Interchromosomal C1 Hi-C contacts between the region on Chromosome 8 (vertical axis) and the entire Chromosome 10. Highlighted region from B indicated in red. End of Chromosome 9 and beginning of Chromosome 11 shown on the left and right side, respectively. **D**: Top: Zoom-in on the C1 Hi-C map of the Chromosome 8/10 amplification unit. Dotted circles indicate enriched "dots" of contacts involving enhancers and *MYC*. Asterisk (*) marks the enhancer-interaction validated in FISH in panels E-F. The dotted line shows the position of the *MYC* gene on Chromosome 8 relative to contacts on Chromosome 10 within the amplification unit. Positions of enhancers from MCF10A indicated as green segments (top and left). Genes shown in red (top and left), with names for selected genes. Bottom: Virtual 4C track (see Methods) showing Hi-C contacts from *MYC* towards the chromosome 10 region for 10A (blue), T1 (yellow) and C1 (green). **E**: FISH image of the *MYC* gene (yellow) and the Chromosome 10 enhancer (blue; Chr. 10 position 73117711-73267436) expected to interact with *MYC* from the Hi-C data, in 10A and C1 cells. Bars, 7 µm. **F**: Quantification of probe-probe distances in pixels, for the *MYC*-Chr10 enhancer probe pair (left; n = 62 [10A] and 269 [C1] observations) and the *MYC*-Chr10 distal probe pair (position 73794997-73992612; n = 62 [10A] and 140 [C1] observations); N = 28-95 nuclei analyzed; P-values are shown (Kolmogorov-Smirnov test).

1458